Classification: Physical Sciences: Environmental Science

Latitudinal gradient in the respiration quotient and the implications for ocean oxygen availability

Allison R. Moreno[1], Catherine A. Garcia[2], Alyse A. Larkin[2], Jenna A. Lee[2], Wei-Lei Wang[2], J. Keith Moore[2], Francois W. Primeau[2], and Adam C. Martiny[1,2,*]

Affiliations:
[1]Department of Ecology and Evolutionary Biology, University of California, Irvine, CA 92697, USA

[2]Department of Earth System Science, University of California, Irvine, CA 92697, USA

[*]**Corresponding Author:**
University of California Irvine, 3208 Croul Hall, CA 92697, USA, Phone: 949-824-9713, Fax: 949-824-3874, amartiny@uci.edu

Keywords: Redfield Ratio, CESM, elemental stoichiometry, inverse modeling, photosynthetic quotient

Abstract:

Climate-driven depletion of ocean oxygen strongly impacts the global cycles of carbon and nutrients as well as the survival of many animal species. One of the main uncertainties in predicting changes to ocean oxygen levels is the regulation of the biological respiration demand associated with the biological pump. Derived from the Redfield ratio, the molar ratio of oxygen to organic carbon consumed during respiration (i.e., the respiration quotient, $r_{-O2:C}$) is consistently assumed constant but rarely, if ever, measured. Using a prognostic Earth system model, we first show that a 0.1 increase in the respiration quotient value leads to a 2.3% decline in global oxygen, a large expansion of low oxygen zones, additional denitrification of 38 Tg N/yr, and overall loss of fixed nitrogen and carbon production in the ocean. We then present direct chemical measurements of $r_{-O2:C}$ using a Pacific Ocean meridional transect crossing all major surface biome types. The observed $r_{-O2:C}$ has a positive correlation with temperature, and regional mean values differ significantly from Redfield proportions. Finally, an independent global inverse model analysis constrained with nutrients, oxygen, and carbon concentrations support a positive temperature dependence of $r_{-O2:C}$ for exported organic matter. We provide evidence against the common assumption of a static biological link between the respiration of organic carbon and the consumption of oxygen. Furthermore, the model simulations suggest that a changing respiration quotient will impact multiple biogeochemical cycles, and that future warming can lead to more intense deoxygenation than previously anticipated.

Significance Statement:

The loss of ocean oxygen caused by climate warming is a serious environmental issue and can lead to major declines in animal habitats. However, current Earth System Models struggle in explaining observed trends in global ocean oxygen. Using a model, we demonstrate that marine oxygen concentrations depend sensitively on a rarely considered quantity known as the respiration quotient to prescribe the oxygen consumed per mole of organic carbon respired. Using a combination of direct chemical measurements across major biomes in the eastern Pacific Ocean plus changes in the global distribution of oxygen and carbon, we show how the respiration quotient increases systematically with temperature. The findings imply that we can experience more intense declines in ocean oxygen with warming.

Introduction:

The oceans are currently experiencing deoxygenation and an expansion of oxygen minimum zones (1) with potentially devastating impacts on marine life (2). Warming induced changes in oxygen solubility as well as circulation-driven ventilation rates are considered the primary drivers of deoxygenation (3). However, current models are unable to reproduce observed shifts in ocean oxygen concentrations (4).

One of the main uncertainties in predicting ocean oxygen levels is the regulation of the biological respiration demand (5). The respiration quotient describes the molar ratio of oxygen to organic carbon consumed during respiration and is thus controlled by the oxidation state of organic material (signified by z) (6):

$$\mathrm{C_x(H_2O)_w(NH_3)_yH_zH_3PO_4} + \left(\mathrm{x} + \tfrac{1}{4}\mathrm{z}\right)\mathrm{O_2} \rightarrow \mathrm{xCO_2} + \mathrm{yNH_3} + \mathrm{H_3PO_4} + \left(\mathrm{w} + \tfrac{1}{2}\mathrm{z}\right)\mathrm{H_2O} \quad (1)$$

$$r_{-O2:C} = \frac{\left(x + \frac{1}{4}z\right)}{x}, \quad (2)$$

with an additional oxygen demand due to nitrification:

$$\mathrm{y\,NH_3} + \mathrm{2y\,O_2} \rightarrow \mathrm{yHNO_3} + \mathrm{yH_2O}, \quad (3)$$

yielding the total respiration quotient ($r_{\Sigma-O2:C}$) describing the full oxidation of particulate organic matter:

$$r_{\Sigma-O2:C} = \frac{\left(x + \frac{1}{4}z + 2y\right)}{x}. \quad (4)$$

The respiration quotient is commonly thought to be static. Alfred Redfield implicitly assumed that all planktonic organic carbon consisted of carbohydrates (setting z to zero) and thus $r_{-O2:C}$ = 1.0 and $r_{\Sigma-O2:C}$ = 1.3 (7). Carbohydrates represent a somewhat oxidized form of organic carbon and other macromolecules (especially lipids) are further reduced with higher

$r_{-O2:C}$. Nevertheless, theoretical estimations of phytoplankton biomass chemistry independently estimated the respiration quotient to be ~1.1 with limited biological variation (8, 9). Finally, a recent analysis using satellite-derived macromolecular composition of phytoplankton and gridded nutrient data was unable to detect any systematic geospatial variation (10). Based on these considerations, ocean biogeochemical models and theories assume a constant respiration quotient although they disagree on the exact value (6).

There is also evidence suggesting substantial variation in the respiration quotient. First, the macromolecular composition of plankton differs across lineages (11) and physiological states (12) leading to a large predicted biological variation in the respiration quotient (SI Appendix, Fig. S1). Second, a limited set of full elemental analyses of particulate organic matter provides support for variation in the carbon oxidation state (13, 14). Third, end-member mixing models of oxygen and DIC concentrations along isopycnal surfaces suggest large variance in $r_{-O2:C}$ between ocean basins (15). However, this method can have large biases (16). Fourth, global inverse model studies find large-scale gradients in $r_{-O2:P}$ and $r_{C:P}$ for the regeneration of organic matter (17, 18). Simply dividing these two ratios suggests that $r_{\Sigma-O2:C}$ could range between 0.7 to 2.1. Such independent studies challenge the notion of a static link between the oxygen and carbon cycles, but the drivers, magnitude, and regional differences of the respiration quotient are unknown.

Here, we report the outcome from a set of prognostic ocean biogeochemical model simulations, direct chemical measurements to estimate the respiration quotient from diverse biomes, and a global inverse model analysis to address the following research questions: (i) what are the global biogeochemical implications of a changing $r_{-O2:C}$, (ii) what is the regional average

and variation in $r_{-O2:C}$, and (iii) does the regional variation in $r_{-O2:C}$ systematically relate to specific environmental conditions?

Results:

A change in the respiration quotient can have widespread impacts on ocean oxygen, nitrogen, and carbon cycle processes. We conducted sensitivity simulations with a prognostic global ocean biogeochemical model (19). The CESM model allowed for variation and dynamical feedbacks between the carbon, nitrogen, oxygen, and phosphorus cycles and included the regulation of primary production, carbon export, and an oxygen dependent water column and sediment denitrification. We specially varied $r_{-O2:C}$ between 0.7 and 1.3 to test for potential biogeochemical impacts of a changing respiration quotient. After a 300 yr spin-up period using unique respiration quotients, we observed nearly linear relationships between $r_{-O2:C}$ and ocean oxygen content, denitrification, and carbon productivity (Fig. 1). The model sensitivity analysis showed that increasing the respiration quotient by 0.1 will results in an average loss of $0.15*10^{18}$ g oxygen (2.3%) and a major expansion of oxygen minimum zones (OMZ, (< 25 μmol/kg O_2) (Fig. 1A-C). The annual rate of denitrification and overall N balance in the ocean were very sensitive to the respiration quotient (Figure 1D-F). Thus, increasing the respiration quotient by 0.1 leads to elevated denitrification of 38 Tg N (45.2%). Denitrification ranged from 3 to 277 Tg N/yr across our simulations but nearly shut down at $r_{-O2:C}$ = 0.7 or rose to very high levels at $r_{-O2:C}$ = 1.3. Indirectly, through the loss of fixed N, an increase in $r_{-O2:C}$ of 0.1 lowered net primary productivity and export production slightly by an average 0.86 (1.59%) and 0.13 (1.56%) Pg C/yr, respectively (Fig 1 G-H). These carbon cycle feedbacks were particularly pronounced on the edge of existing the OMZs. Thus, the respiration quotient is an important regulator of marine biogeochemical cycles.

The changes to ocean biogeochemical cycles from a varying respiration quotient are comparable in magnitude to business-as-usual climate change impacts by year 2100 (SI Appendix, Fig. S2 and Table S1). Climate simulations performed under scenario RCP8.5 showed a decline in the total dissolved oxygen content of the ocean between 3.1% and 4.7% by year 2100. We see equivalent changes in CESM simulations a change in $r_{-O2:C}$ of ~0.2 (Fig. 1). Therefore, a shift in the respiration quotients can significantly impact ocean oxygen levels and biogeochemical cycles more broadly.

To directly quantify the respiration quotient, we combined field measurements of particulate organic carbon (POC) and the required oxygen demand for respiration across a meridional transect in the Eastern Pacific Ocean. POC was estimated by combustion and the release of CO_2 using an elemental analyzer. To quantify the oxygen required for complete respiration of POC, we modified and calibrated a method commonly used for measuring the particulate chemical oxygen demand (PCOD) in wastewater (20). We then estimated the respiration quotient ($r_{-O2:C}$) by taking the ratio of PCOD and POC across 198 stations along the Pacific Ocean line P18 (SI Appendix, Table S2). Sea-surface temperature steadily decreased from 29.5°C to approximately 0°C (Fig. 2A). A deep nutricline was detected in multiple regions marking the location of subtropical gyre conditions (Fig. 2B). Nitrate was mostly drawn down to detection limit in several regions, whereas residual phosphate was present throughout the Eastern Pacific Ocean (SI Appendix, Fig. S4). As a result, N* was low in most of the tropical and subtropical regions but rose with the high nutrient supply in the Southern Ocean (Fig. 2C). As such, our samples covered a broad range of environmental conditions across the eastern Pacific Ocean.

We observed distinct but highly correlated POM concentration levels across the regions. [POC] and [PCOD] were tightly correlated ($r^2_{Pearson}$ = 0.93, $p < 0.0001$) (Fig. 2D, E) and showed parallel regional shifts. Thus, our optimized PCOD assay accurately reflects the concentration of marine particulate organic matter. [POC] and [PCOD] were both low in the gyre regions (1:CAMR, 2:PNEC, 3:TPEC, and 5:SPSG), slightly higher in equatorial Pacific Ocean waters (4:PEQD), and very high in the Southern Ocean regions (6:SST – 9:APLR) (Fig. 2D, E). Changes in POM concentrations followed the nine regions that arose from the combination of environmental conditions. $r_{-O2:C}$ averaged $1.15^{1.54}_{0.73}$ (minimum and maximum value) (Fig. 2F, SI Appendix, Table S3) but differed significantly between regions ($p_{MANOVA} < 6*10^{-5}$) (Fig. 3). The highest and lowest regional averages were found near the warm edge of the North Pacific Subtropical Gyre and the ice edge in the Southern Ocean, respectively. The equatorial regions were also slightly lower compared to the two gyres. Many regions showed limited overlap with the respiration quotient defined by Redfield and Anderson but instead largely grouped along a latitudinal gradient (Fig. 3). Thus, the observed respiration quotient showed regional shifts leading to a common divergence from past predicted values.

We observed a significant correspondence between ocean environmental conditions and the respiration quotient. We tested all linear combinations of environmental factors and $r_{-O2:C}$ (SI Appendix, Table S4). A significant positive relationship between temperature and $r_{-O2:C}$ suggested an increase in $r_{-O2:C}$ of ~ 0.2 between polar and tropical regions (Fig. 4A). We saw indications of an additional regulation of $r_{-O2:C}$ by nutrient availability (SI Appendix, Table S4). A deeper nutricline led to a slightly elevated quotient in comparison to waters with the same temperature but higher nutrients (e.g., the equatorial region). A positive relationship between temperature and the respiration quotient was also observed for a small set of previously analyzed

samples from the Western North Pacific Ocean (SI Appendix, Fig. S5). Temperature emerged as the best predictor, but additional factors may exert a secondary control on the respiration quotient.

We tested if the observed temperature dependence of $r_{-O2:C}$ could be detected via the imprint on the global three-dimensional distribution of oxygen and dissolved inorganic carbon in the ocean. To achieve this, we constructed an inverse biogeochemical model constrained by the GLODAP.2016v2 and WOA2013 databases of hydrographic measurements of nutrients, carbon, and oxygen concentrations (21, 22). We relied on previous inverse-modeling efforts for the carbon, nitrogen, and phosphorus cycles (18, 19, 23) but with an added oxygen cycling model. The resulting biogeochemical model tracks the dissolved oxygen concentration as well as the oxidation and reduction of both nitrogen and carbon. Based on the direct chemical measurements, we introduced a linear temperature dependence of the respiration quotient but with unknown slope and intercept. We then estimated $r_{-O2:C} = 0.974^{0.980}_{0.968}$ at 15°C (± 1 std) and a positive temperature dependence of $0.0162^{0.0167}_{0.0157}$°C^{-1} through a Bayesian inversion procedure against the global 3-D distribution of nutrients, carbon, and oxygen concentrations (Fig. 4B). The temperature dependence of $r_{-O2:C}$ from the inverse model is stronger and lower in colder waters. However, the chemical measurements and inverse hydrographic estimate both agree on the positive temperature relationship and the level at higher temperature (Fig. 4). We also evaluated a nitrate-based model for $r_{-O2:C}$, but there was stronger support for a temperature dependence (see supplementary information). We allowed for independent remineralization depth profiles (Martin's b) of POC and PCOD. b_{Oxygen} was slightly smaller than b_{Carbon} suggesting that oxygen was consumed deeper in the water column compared to the release of DIC. However, the uncertainty in each parameter led to overlapping values, so it was unclear if the carbon and

oxygen remineralization profiles were truly distinct. The midpoint value of $r_{-O2:C}$ at 15˚C was also sensitive to the inclusion of separate Martin's *b* values for POC and PCOD. A separate inverse model with a common depth profile for POC and PCOD yielded a mean $r_{-O2:C}$ value of 1.12, which is in better agreement with the value measured directly in suspended particles. This link suggested some poorly constrained model interactions between the mean respiration quotient and the remineralization depth profiles. However, the positive temperature dependence of $r_{-O2:C}$ was retained independently of how we parameterized remineralization depth profiles. In summary, we have convergent estimates of a regional temperature-related respiration quotient but uncertainty in the magnitude of change.

Discussion

The observed range for the respiration quotient is slightly outside the bounds of predictions based on cellular biochemistry (8, 9). However, the C:H:O ratio of POM in the Western Pacific Ocean corresponds to a respiration quotient ranging between 0.6 and 1.6 (13) and several studies have detected 40% variation in C:H (24). Platt and Irwin observed a 30% variation in the caloric content of fresh organic matter (25). As the carbon oxidation state and caloric content of organic matter are closely tied (24), one should expect a parallel range in the respiration quotient. Part of POM is detrital matter with molecularly uncharacterized components (26) that could lead to higher $r_{-O2:C}$ variation than predicted purely from cellular biochemistry arguments. The observed values are also within the bounds from endmember mixing models (15) and other POM analyses (13). Thus, our detected range in $r_{-O2:C}$ is high but falls within past observation of particulate organic matter.

The observed latitudinal gradient for the respiration quotient must be linked to changes in the underlying molecular composition of surface POM and plankton. The exact nature of this

relationship remains to be quantified, but we expect it is driven by an increased proportion of lipids relative to proteins and carbohydrates. The plankton communities are distinct between the analyzed regions in the eastern Pacific Ocean suggesting that environmentally-driven community shifts at least partially contribute to the variation in the respiration quotient. The proportion of biochemical components across major phytoplankton groups follow an allometric relationship leading to an elevated lipid-to-carbohydrate/protein ratio in small plankton (27). We speculate that smaller cells have a higher contribution of the lipid-rich membrane to total carbon due to the elevated surface-to-volume ratio. Thus, the high abundance of small picoplankton in warm tropical and subtropical regions could therefore lead to a higher lipid fraction and higher respiration quotient of the organic matter. Another biological mechanism is the accumulation of lipids following a nitrogen starvation response in many phytoplankton (28), and we observed the highest respiration quotient in warm regions with a deep nutricline. Thus, we hypothesize that shifts in plankton biogeography and possibly physiology influence the observed changes in the respiration quotient.

There are several noteworthy caveats to our conclusions. First, the POM oxidative state may change during sinking and aging leading to distinct remineralization length scales for DIC release and oxygen consumptions. From the inverse model, we saw weak evidence for a faster attenuation of DIC compared to oxygen consumption suggesting a removal of oxidized compounds in the upper ocean. The confidence intervals for b_{Carbon} and b_{Oxygen} were overlapping but future vertical joint profiles of POC and PCOD could further constrain any depth dependence of the respiration quotient. Second, we did not measure the respiration quotient of DOM even though this fraction is an important component of the ocean carbon cycle (29). Currently, no analytic methods can perform this measurement directly, so it is unclear if $r_{-O2:C}$ for POM and

DOM will display the same level and biome patterns. Third, the simulated impact of a changing respiration quotient was limited to 300 yrs, so additional feedbacks could occur at longer time-scales. Within the time-scale most relevant to human society, the model analysis clearly emphasized the linear impact of the respiration quotient on ocean oxygen levels and downstream biogeochemical cascade. Fourth, our observed variation in the respiration quotient in suspended POM and inferred from the inverse model show variability that was not detected in a recent study (10). In this recent study, the respiration quotient was estimated by combining satellite-predicted macromolecular composition of surface POM and using a simple 1-D model of hydrographic nutrient and oxygen measurements. This recent work may have lacked the sensitivity to detect regional shifts in $r_{-O2:C}$, as the lateral transport of nutrients and oxygen tends to dominate over 1-D vertical transport in the ocean. Thus, our combination of a data-constrained 3-D biogeochemical model (30) and direct POM measurements may be more sensitive for detecting a temperature dependence of $r_{-O2:C}$. Fifth, there is uncertainty embedded in our transport operator as well as in the global annual climatological description of hydrography that can impact the inverse model estimates. Seasonally resolved transport and biogeochemistry as well as expanded oxygen measurements from Biogeochemical-Argo floats will help further constrain future estimates of $r_{-O2:C}$. Sixth, $r_{-O2:C}$ may be related to additional parameters beyond temperature. For example, we saw indications of some impact of nutrient availability (although not as strong as temperature) as well as signs of daily variance possibly reflecting diel cycles in photosynthesis and cellular carbon accumulation. These sources of additional variance need to be addressed with expanded regional, vertical, and temporal sampling in future studies. The uncertainty estimates we have provided from our inverse model analysis are conditioned on the model structure. Exploring more complex relationships between $r_{-O2:C}$ and a broader suite of

drivers in the lab, *in situ*, and by the inverse model should improve our understanding of how the respiration quotient is regulation. Nevertheless, our use of independent methods supports that the respiration quotient is not to be assumed constant but varies between biomes.

The observed variation in the respiration quotient is expected to have large biological and biogeochemical impacts. The production of more reduced organic carbon in tropical and subtropical regions implies a higher caloric content and perhaps a superior food source (24). On the other hand, we see that an upshift in the respiration quotient can initiate a biogeochemical cascade leading to lower ocean oxygen levels, N loss, and declining productivity. These biogeochemical changes could have devastating impacts on marine life (2). Thus, a biological feedback whereby warming and stratification leads to the production of more reduced organic carbon can have a large future impact on marine ecosystem functioning and biogeochemistry.

Materials and Methods

Sample Collection: Seawater samples were collected during the GO-SHIP P18 cruise aboard R/V *Ronald H. Brown* from November 11, 2016 to February 3, 2017 between 32.72° N, 117.16°W off San Diego, CA to 77.85°S, 166.67°E near Antarctica (SI Appendix, Fig. S3). Samples for particulate organic carbon (POC) and particulate chemical oxygen demand (PCOD) were taken from 198 stations using the underway system. The underway intake was located at a depth of 5.3 m from the sea surface. All carboys were rinsed twice with filtered seawater before sampling. Triplicate samples for POC and sextuplicate samples for PCOD were taken approximately 3 times daily. Water was pre-filtered with a 30 μm nylon mesh (Small Parts #7050-1220-000-12) to remove rare large particles from the sample. Additional samples (triplicate for POC and sextuplicate for PCOD) were taken by removing the 30 μm nylon mesh, allowing all particles to collect in order to determine the total particulate organic matter from

station 159 to 198. All samples were collected on pre-combusted 500°C GF/F filters (Whatman, GE Healthcare, Little Chalfont, Buckinghamshire, UK) for the analysis of POC and PCOD. Sample volume was determined on a per station basis, ranging from 3 to 8 l. All filters were then folded in half, sealed inside pre-combusted aluminum foil, and stored at -20°C until analysis.

Particulate Organic Carbon (POC). Filters were dried at 55°C (24 h) and then stored in a desiccator with concentrated hydrochloric acid fumes for 24 h to remove inorganic carbonates. The filters were dried for 48 h at 55°C before being folded and pelletized into pre-combusted tin capsules (CE Elantech, Lakewood, New Jersey). Tin capsules were then analyzed on a Flash EA 1112 NC Soil Analyzer (Thermo Scientific, Waltham, Massachusetts) measuring released CO_2 and we used an atropine ($C_{17}H_{23}NO_3$) standard.

Particulate Chemical Oxygen Demand (PCOD) Assay: Quantifying the Chemical Oxygen Demand is commonly used for wastewater and freshwater samples. The assay is based on the determination of residual potassium dichromate following organic matter oxidation with silver sulfate as catalyst under strongly acidic and high temperature (150°C) conditions (20, 31, 32). As dichromate does not oxidize ammonium, the assay only quantifies the oxygen demand from organic carbon. A major obstacle for using the method with seawater POM samples is the interference of chloride ions. As such, chloride is oxidized by dichromate and causes precipitation of silver chloride. Several efforts have been made to apply this method to seawater samples and the main solution is the addition of mercuric sulfate (33). Thus, the method has the potential for quantifying the oxygen demand in marine POM.

Here, we modified the assay to quantify the chemical oxygen demand from POM collected on GF/F filters. Specifically, GF/F filters with collected POM samples were dried overnight at 55°C. We then added the filter and 2 ml milli-Q water to HACH COD HR+ reagent

vials (Product # 2415915 containing mercuric sulfate) and digested the samples at 150˚C for 2 h. We learned that the major obstacle for this assay was uneven precipitation of silver chloride following digestion. Thus, we modified the assay to include a subsequent precipitation step by adding 92.1 μL of 9.5 M NaCl (minimum amount of chloride to induce consistent precipitation) to each vial. Vials were immediately inverted twice and centrifuged for 30 min at 2500 rpm to remove any precipitate. Finally, we quantified the remaining dichromate by absorbance at 600 nm using HACH certified phthalate-based COD standards (SI Appendix, Fig. S6A). HACH certified COD tubes have been shown to measure unbiased COD across diverse classes of organic compounds (34) so we only did a limited comparison with other compounds.

To validate the modified technique, we (i) tested for any interference using standard additions of a HACH certified phthalate-based COD standard, (ii) established a linear relationship between input amounts and absorbance, (iii) compared the variance to other POM measurement techniques, and (iv) examined any compound specific biases. First, we were able to recover experimentally added organic carbon to seawater samples suggesting limited sample interference (SI Appendix, Fig. S6B). Second, we found that increasing sample volume (and associated amount of PCOD captured on filters) corresponded linearly to an increase in measured PCOD (SI Appendix, Fig. S6C). Third, we saw a high correspondence between theoretical and observed values for different substrates (SI Appendix, Fig. S6D). This has also been observed in more elaborate past studies supporting that the dichromate technique effectively oxidizes many diverse substrates (34, 35). Fourth, the coefficient of variance for PCOD and $r_{-\mathrm{O2:C}}$ corresponded to the coefficient of variance for POC and $r_{C:P}$, respectively (SI Appendix, Fig. S6E-H). We did not fully explore the detection limit for our assay as the COD chemistry method was much more sensitive than one used for POC. Thus, our sampling strategy

focused on recovering enough POC. These method development and optimization steps suggested that our assay provided an unbiased and sensitive method to quantify PCOD.

$r_{-O2:C}$ was computed from the mean concentrations of PCOD and POC. The standard deviation for $r_{-O2:C}$ was calculated as a pooled sample:

$$\sigma_{r_{-O2:C}} = \frac{PCOD_{aver}}{POC_{aver}} \times \sqrt{\left(\left(\frac{\sigma_{PCOD}}{POC_{aver}}\right)^2 + \left(\frac{\sigma_{POC}}{POC_{aver}}\right)^2\right)}. \quad (5)$$

The coefficient of variance was calculated as a pooled sample:

$$cv_{r-O2:C} = \frac{\sigma_{r-O2:C}}{r_{-O2:C,aver}}. \quad (6)$$

Statistical linear models were fitted using one or two predictor variables (Temperature (°C; T), Nutricline Depth (m; Z_{NO3} = 1 µM NO_3), Phosphate (P), and N* (N* = [NO3] – 16*[P] + 2.9 mmol/m^3). To evaluate assumptions of a normal-distributed respiration quotient, we also did a 1-way 'multi-variate analysis of variance' (MANOVA) test. Here, we evaluated the joint variance in POC and PCOD between the nine defined regions. We rejected the hypothesis that the data could be described in one dimension (i.e., a single mean $r_{-O2:C}$) and instead showed significant regional variability.

Our standard POM assay quantifies particles less than 30 µm to avoid the stochastic presence of rare large particles. However, large phytoplankton are an important contributor to POM in the Southern Ocean. To address any uncertainties with size selection, we also collected POM with no size fractionation between 54° S and 69° S (SI Appendix, Fig. S7A). We found that total [POC] or [PCOD] were only significantly different from the <30 µm fraction at a few stations. Furthermore, $r_{-O2:C}$ was not statistically different between the total and below <30 µm fractions. This suggested that capping the POM sample at a particle size of 30 µm did not affect the outcome of our analysis (SI Appendix, Fig. S7C).

Prognostic CESM Simulations: A modified version of Community Earth System Model (CESM) was used for our 300-year simulations, which included a prescribed $r_{-O2:C}$ ranging between 0.7 and 1.3 across model experiments. Only a fixed $r_{-O2:C}$ value varied between these simulations. Climate forcings on the oceans followed a repeated cycling of the NCEP-NCAR Reanalysis datasets for the years 1980-2009. Three hundred years is sufficient to spin up the upper ocean and thermocline depth nutrients and oxygen. Model output was averaged over the last 20 simulation years for analysis to remove short-term variability. The model includes three phytoplankton functional groups (small, large, and diazotrophic phytoplankton) and multiple potentially growth-limiting nutrients (N, P, Fe, Si). The model has been used in CESM climate simulations (36, 37). The ecosystem-biogeochemistry model code is a preliminary version of the CESM V2.1 code set, run within the coarse-resolution CESM V1.2.2 ocean circulation model (19). Water column denitrification is initiated in the model when oxygen levels fall below 7 μM, with only denitrification and no oxic remineralization below 5 μM (36). Additional documentation and model source code for CESM2.0 are available online (www2.cesm.ucar.edu).

Analysis of CMIP5 Model Output: We obtained output from the Coupled Model Intercomparison Project Phase 5 (CMIP5) models from the Earth System Grid Federation (38). We calculated the changes in ocean oxygen content and rates of denitrification between the simulated 1990s and 2090s for available biogeochemical models following the historical and Representative Concentration Pathway 8.5 (RCP8.5). This is the high-end, business as usual, emissions scenario with strong global warming over the 21st century.

Inverse Hydrographic Model Analysis: See the supplementary information for a detailed description of the inverse model analysis.

Data availability: The hydrography (https://cchdo.ucsd.edu/cruise/33RO20161119) and POM data (https://www.bco-dmo.org/project/764270) are freely available.

Acknowledgement

We thank the captain and crew of the R/V *Ronald H. Brown*, the chief scientist B. Carter and R. Sonnerup, and the science party on board the P18 cruise. We also thank GO-SHIP coordinators Lynne Talley and Gregory Johnson for their support in participating in the U.S. Global Ocean Carbon and Repeat Hydrography Program. This research was developed as part of Allison Moreno's dissertation "Biological Controls and Biogeochemical Outcomes of Marine Elemental Stoichiometry." **Funding:** National Science Foundation GRFP and UCI Chancellor's Club Fellowship to ARM, OCE-1848576 and OCE- 1948842 to ACM and FWP, National Aeronautics and Space Administration Earth and Space Science Fellowship NESSF16R to CAG, US Department of Energy Office of Biological and Environmental Research awards DE-SC0016329, DE-SC0016539, and RUBISCO SFA to JKM.

Figure legends

Figure 1. Impact of a changing respiration quotient on ocean biogeochemical processes. **A**. Change in OMZ ($O_2 \leq 25$ μM) extent and intensification when $r_{-O2:C}$ shifts from 1 to 0.7. **B**. Change in OMZ extent and intensification when $r_{-O2:C}$ shifts from 1 to 1.3. **C**. Total oxygen levels and OMZ volume ($[O_2] < 25$μM) as a function of the respiration quotient. **D**. Change in denitrification zones and intensity when $r_{-O2:C}$ shifts from 1 to 0.7. **E**. Change in denitrification zones and intensity when $r_{-O2:C}$ shifts from 1 to 1.3. **F**. Annual denitrification rates and global ocean N balance as a function of the respiration quotient. **G**. Change in ocean net primary production when $r_{-O2:C}$ shifts from 1 to 0.7. **H**. Change in ocean net primary production when $r_{-O2:C}$ shifts from 1 to 1.3. **I.** Annual net primary production and carbon export (at 100 m) as a function of the respiration quotient.

Fig 2. Environmental conditions, POM concentrations and the respiration quotient across the eastern Pacific Ocean. **A.** Sea-surface temperature, **B.** Nutricline depth (depth at which nitrate is 1 μM), **C.** Surface N* ($N^* = NO^{-3}_{Station} - 16*PO4^{-3}_{Station}$), **D.** Surface particulate organic carbon (POC), **E.** Surface particulate chemical oxygen demand (PCOD), and **F.** Surface respiration quotient. Averaged data are marked as black dots. In panels A-E, the red line represents a 4-station moving average. In panels D-F, the grey shaded regions represent the standard deviation of the replicates. In panel F, the red line represents an 8-station moving average. In all panels, the colored background represents the nine regions (1:CAMR- Central American Coast, 2: PNEC- North Pacific Equatorial Counter Current, 3:TPEQ- Transitional

Pacific Equatorial Divergence, 4: PEQD- Pacific Equatorial Divergence, 5:SPSG- South Pacific Gyre, 6:SST- Southern Subtropical Convergence, 7:SANT- Sub Antarctic water ring, 8: ANTA- Antarctic, 9: APLR- Austral Polar).

Figure 3. Regional differences in the respiration quotient. **A.** Clustering of group means after a multivariate joint POC and PCOD analysis of variance (1-way MANOVA). **B.** Regionally observed respiration quotients and comparisons to Redfield ($r_{-O2:C}$ = 1) and Anderson ($r_{-O2:C}$ = 1.1) theoretically predicted values.

Figure 4. Relationship between temperature and the respiration quotient. A. Observed temperature dependence for surface POM $r_{-\mathrm{O2:C}}$ = 1.0465 + (0.0055383/℃) *SST* (Table S4) and the relationship inferred from the inversion of hydrographic data (Table S6). **B.** The logarithmic marginal posterior probability density for the temperature dependence (m) and intercept (b) in the relationship $r_{-\mathrm{O2:C}} = m(SST - 15℃) + b$ estimated from the inversion of the hydrographic data.

References:

1. S. Schmidtko, L. Stramma, M. Visbeck, Decline in global oceanic oxygen content during the past five decades. *Nature* **542**, 335–339 (2017).
2. R. J. Diaz, R. Rosenberg, Spreading dead zones and consequences for marine ecosystems. *Science* **321**, 926–929 (2008).
3. R. E. Keeling, A. Körtzinger, N. Gruber, Ocean deoxygenation in a warming world. *Ann. Rev. Mar. Sci.* **2**, 199–229 (2010).
4. L. Stramma, A. Oschlies, S. Schmidtko, Mismatch between observed and modeled trends in dissolved upper-ocean oxygen over the last 50 yr. *Biogeosciences* **9**, 4045–4059 (2012).
5. A. Oschlies, P. Brandt, L. Stramma, S. Schmidtko, Drivers and mechanisms of ocean deoxygenation. *Nat. Geosci.* **11**, 467–473 (2018).
6. A. Paulmier, I. Kriest, A. Oschlies, Stoichiometries of remineralisation and denitrification in global biogeochemical ocean models. *Biogeosciences* **6**, 923–935 (2009).
7. A. C. Redfield, B. H. Ketchum, F. A. Richards, "The influence of organisms on the composition of sea-water" in *The Sea, Vol.2, Interscience Publishers, New York*, M. N. Hill, Ed. (John Wiley, 1963), pp. 26–77.
8. L. A. Anderson, On the hydrogen and oxygen content of marine phytoplankton. *Deep Sea Res. Part I Oceanogr. Res. Pap.* **42**, 1675–1680 (1995).
9. E. A. Laws, P. G. Falkowski, W. O. Smith, H. Ducklow, J. J. McCarthy, Temperature effects on export production in the open ocean. *Global Biogeochem. Cycles* **14**, 1231–1246 (2000).
10. T. Tanioka, K. Matsumoto, Stability of Marine Organic Matter Respiration Stoichiometry. *Geophys. Res. Lett.* **47** (2020).
11. Z. V Finkel, *et al.*, Phylogenetic diversity in the macromolecular composition of microalgae. *PLoS One* **11**, e0155977 (2016).
12. F. Fraga, A. F. Rios, F. F. Perez, F. G. Figueiras, Theoretical limits of oxygen:carbon and oxygen:nitrogen ratios during photosynthesis and the mineralization of the organic matter inthe sea. *Sci. Mar.* **62**, 161–168 (1998).
13. C. T. A. Chen, C. M. Lin, B. T. Huang, L. F. Chang, Stoichiometry of carbon, hydrogen, nitrogen, sulfur and oxygen in the particulate matter of the western North Pacific marginal seas. *Mar. Chem.* **54**, 179–190 (1996).
14. J. I. Hedges, *et al.*, The biochemical and elemental compositions of marine plankton: A NMR perspective. *Mar. Chem.* **78**, 47–63 (2002).
15. Y.-H. Li, T.-H. Peng, Latitudinal change of remineralization ratios in the oceans and its implication for nutrient cycles. *Global Biogeochem. Cycles* **16**, 77-1-77–16 (2002).
16. B. Schneider, J. Karstensen, A. Oschlies, R. Schlitzer, Model-based evaluation of methods to determine C:N and N:P regeneration ratios from dissolved nutrients. *Global Biogeochem. Cycles* **19**, 1–18 (2005).
17. T. DeVries, C. Deutsch, Large-scale variations in the stoichiometry of marine organic matter respiration. *Nat. Geosci.* **7**, 890–894 (2014).
18. Y.-C. Teng, F. W. Primeau, J. K. Moore, M. W. Lomas, A. C. Martiny, Global-scale variations of the ratios of carbon to phosphorus in exported marine organic matter. *Nat. Geosci.* **7**, 895–898 (2014).
19. W. Wang, J. K. Moore, A. C. Martiny, F. W. Primeau, Convergent estimates of marine nitrogen fixation. *Nature* **566**, 205–211 (2019).
20. I. Vyrides, D. C. Stuckey, A modified method for the determination of chemical oxygen

demand (COD) for samples with high salinity and low organics. *Bioresour. Technol.* **100**, 979–982 (2009).
21. R. M. Key, *et al.*, Global Ocean Data Analysis Project, Version 2 (GLODAPv2) (2015).
22. A. Olsen, *et al.*, The Global Ocean Data Analysis Project version 2 (GLODAPv2) – an internally consistent data product for the world ocean. *Earth Syst. Sci. Data* **8**, 297–323 (2016).
23. F. W. Primeau, M. Holzer, T. DeVries, Southern Ocean nutrient trapping and the efficiency of the biological pump. *J. Geophys. Res. Ocean.* **118**, 2547–2564 (2013).
24. D. M. Karl, E. Grabowski, The importance of H in particulate organic matter stoichiometry, export and energy flow. *Front. Microbiol.* **8**, 1–7 (2017).
25. T. Platt, B. Irwin, Caloric content of phytoplankton. *Limnol. Oceanogr.* **18**, 306–310 (1972).
26. J. I. Hedges, *et al.*, The molecularly-uncharacterized component of nonliving organic matter in natural environments. *Org. Geochem.* **31**, 945–958 (2000).
27. Z. V. Finkel, M. J. Follows, A. J. Irwin, Size-scaling of macromolecules and chemical energy content in the eukaryotic microalgae. *J. Plankton Res.* **38**, 1151–1162 (2016).
28. N. S. Shifrin, S. W. Chisholm, Phytoplankton lipids: interspecific differences and effects of nitrate, silicate and light-dark cycles. *J. Phycol.* **17**, 374–384 (1981).
29. S. Roshan, T. Devries, Efficient dissolved organic carbon production and export in the oligotrophic ocean. *Nat. Commun.* **8** (2017).
30. J. B. Palter, M. S. Lozier, R. T. Barber, The effect of advection on the nutrient reservoir in the North Atlantic subtropical gyre. *Nature*, 687–692 (2005).
31. W. A. Moore, R. C. Kroner, C. C. Ruchhoft, Dichromate reflux method for determination of oxygen consumed. *Anal. Chem.* **21**, 953–957 (1949).
32. F. J. Baumann, Dichromate reflux chemical oxygen demand. Proposed method for chloride correction in highly saline wastes. *Anal. Chem.* **46**, 1336–1338 (1974).
33. R. A. Dobbs, R. T. Williams, Elimination of chloride interference in the chemical oxygen demand test. *Anal. Chem.* **35**, 1064–1067 (1963).
34. J. R. Baker, M. W. Milke, J. R. Mihelcic, Relationship between chemical and theoretical oxygen demand for specific classes of organic chemicals. *Water Res.* **33**, 327–334 (1999).
35. Y. C. Kim, *et al.*, Relationship between theoretical oxygen demand and photocatalytic chemical oxygen demand for specific classes of organic chemicals. *Analyst* (2000).
36. J. K. Moore, K. Lindsay, S. C. Doney, M. C. Long, K. Misumi, Marine ecosystem dynamics and biogeochemical cycling in the Community Earth System Model [CESM1 (BGC)]: Comparison of the 1990s with the 2090s under the RCP4. 5 and RCP8. 5 scenarios. *J. Clim.* **26**, 9291–9312 (2013).
37. J. K. Moore, *et al.*, Sustained climate warming drives declining marine biological productivity. *Science* **359**, 1139–1143 (2018).
38. K. E. Taylor, R. J. Stouffer, G. A. Meehl, An overview of CMIP5 and the experiment design. *Bull. Am. Meteorol. Soc.* **93**, 485–498 (2012).

PNAS
www.pnas.org

Supplementary Information for

Latitudinal gradient in the carbon-to-oxygen respiration quotient and the implications for ocean oxygen availability

Allison R. Moreno[1], Catherine A. Garcia[2], Alyse A. Larkin[2], Jenna A. Lee[2], Wei-Lei Wang[2], J. Keith Moore[2], Francois W. Primeau[2], and Adam C. Martiny[1,2,*]

[1]Department of Ecology and Evolutionary Biology, University of California, Irvine, CA 92697, USA
[2]Department of Earth System Science, University of California, Irvine, CA 92697, USA

* **Corresponding Author**
University of California Irvine, 3208 Croul Hall, CA 92697, USA, Phone: 949-824-9713, Fax: 949-824-3874
Email: amartiny@uci.edu

This PDF file includes:

Supplementary text
Figures S1 to S8
Tables S1 to S8
SI References

Supplementary Information Text

Inverse Biogeochemical Model Methods:

Our biogeochemistry model predicts the concentrations of oxygen, dissolved inorganic carbon, and dissolved organic carbon ($[\mathrm{O}_2]$, $[\mathrm{DIC}]$, and $[\mathrm{DOC}]$), as a function of $r_{-\mathrm{O2:C}}$, which in turn is parameterized in terms of either surface temperature or surface nitrate concentration, via a slope, *m,* and intercept, *b:*

$$r_{-\mathrm{O2:C}} = mz + b, \tag{S1}$$

with

$$\text{MODEL A: } z = z_A \equiv \frac{SST - \mu_{SST}}{\Delta_{SST}}, \tag{S2}$$

or

$$\text{MODEL B: } z = z_B \equiv \frac{SSN - \mu_{SSN}}{\Delta_{SSN}}, \tag{S3}$$

where SST is the sea surface temperature and SSN is the sea surface nitrate concentration obtained from the 2013 World Ocean Atlas [Ref. S1]. The means μ_{SST} and μ_{SSN} are computed using an area weighted average of the *SST* and *SSN* variables after interpolation onto the global 2° x 2° grid. For the scale parameters we use

$$\Delta_{SST} = \max SST - \min SST, \tag{S4}$$

and

$$\Delta_{SSN} = \max SSN - \min SSN, \tag{S5}$$

so that

$$\frac{d}{dm}[\min r_{-\mathrm{O2:C}} - \max r_{-\mathrm{O2:C}}] = 1, \tag{S6}$$

for both model A and model B. In Table S5, we list the values of the quantitates used to standardize the SST and SSN variables and compare the range of SST and SSN to their respective standard deviations.

The biogeochemical model is also dependent on four additional parameters (b_C, b_O, κ_{dC}, and σ described later) and associated uncertainty. An important advantage of the Bayesian inversion procedure is that it allows us to marginalize out the parameters that are not of direct of interest, namely b_C, b_O, κ_{dC}, and σ and thus take into account their uncertainty in the posterior uncertainty for $r_{-\mathrm{O2:C}}$. Another important advantage of the Bayesian procedure is the ability to compute the probability of model A relative to B and thus decide if the spatial variability of $r_{-\mathrm{O2:C}}$ is better parameterized as a function SST or SSN. Both model A and model B share the same number of parameters making the Bayesian model selection process particularly transparent and easy to interpret.

The nitrogen-cycle model of Wang et al. (2019): The formulation of our biogeochemical model builds on the nitrogen-cycle model of Ref. S2. This model uses the data-constrained circulation model of Ref. S3 coupled to a nitrogen and phosphorus cycling model to predict the global distribution of organic nitrogen production, benthic denitrification and water column denitrification. The circulation model has a horizontal resolution of 2° × 2° with 24 layers ranging in thickness from 36 m near the surface to 633.5 m near the bottom. In total, the model has $n_{mod} = 191{,}169$ wet grid boxes. From this model we extract the following variables:

- P_{Norg}: the rate of organic nitrogen production.
- D_{wc}: the rate of water column fixed N loss due to denitrification and annamox.
- D_{sed}: the rate of benthic fixed N loss due to denitrification and annamox.
- $1 - R$: the fraction of organic nitrogen production associated with external N inputs, including microbial $\mathrm{N_2}$fixation, riverine input and atmospheric deposition.

These variables are then used to drive the carbon and oxygen cycling model as explained below.

The governing equations for $[\mathrm{O_2}]$: The governing equation for the concentration of dissolved oxygen in the ocean is given by

$$\left[\frac{d}{dt} + \mathbf{T}\right][\mathrm{O}_2] = P_{O2} - L_{O2} + \mathbf{K}_{O2}([\mathrm{O}_2]_{sat} - [\mathrm{O}_2]), \quad \text{(S7)}$$

Where $\mathbf{T}$ is the advection-diffusion transport operator defined such that

$$\mathbf{T}c \equiv \nabla \cdot [\boldsymbol{u}c - \boldsymbol{\kappa}\nabla c], \quad \text{(S8)}$$

subject to no-flux boundary conditions at the basin boundaries and the sea surface. With this definition, $\boldsymbol{u}$ is the residual mean circulation and $\boldsymbol{\kappa}$ is the eddy-diffusion tensor. $\mathbf{K_{O2}}$ is the air-sea gas-exchange operator and $[\mathrm{O}_2]_{sat}$ is the saturation concentration of a surface water parcel in equilibrium with the atmosphere. We use the OCMIP-2 air-sea gas exchange formulation (http://ocmip5.ipsl.jussieu.fr/OCMIP/phase2/simulations/). P_{O2} and L_{O2} are the biological production and loss of oxygen due to photosynthesis and respiration, respectively. If we assume that the ocean is in a climatological steady state, the three-dimensional oxygen distribution is given by

$$[\mathrm{O}_2]_{\mathrm{mod}} = [\mathbf{T} + \mathbf{K_{O2}}]^{-1}(P_{O2} - L_{O2} + \mathbf{K_{O2}}[\mathrm{O}_2]_{\mathrm{sat}}). \quad \text{(S9)}$$

The production of photosynthetic O_2: We will use the stoichiometric ratios x, y, and z defined from the chemical formula for the respiration of organic matter

$$\mathrm{C}_x(\mathrm{H}_2\mathrm{O})_w(\mathrm{NH}_3)_y\mathrm{H}_z\mathrm{H}_3\mathrm{PO}_4 + \left(x + \frac{1}{4}z\right)\mathrm{O}_2 \rightarrow x\mathrm{CO}_2 + y\mathrm{NH}_3 + \mathrm{H}_3\mathrm{PO}_4 + \left(w + \frac{1}{2}z\right)\mathrm{H}_2\mathrm{O}, \quad \text{(S10)}$$

and the oxidation of ammonia to nitrate

$$y\mathrm{NH}_3 + 2y\mathrm{O}_2 \rightarrow y\mathrm{HNO}_3 + y\mathrm{H}_2\mathrm{O}. \quad \text{(S11)}$$

In other words, x and y are, respectively, the relative number of moles carbon dioxide and ammonia produced by the respiration of organic matter, and z represents an anomaly in the number of H atoms that get oxidized into $\mathrm{H}_2\mathrm{O}$ per mole of organic C.

Using these ratios, the rate of photosynthetic O_2 production can be expressed in terms of the rate of organic-nitrogen production (P_{Norg}) and the fraction $(1 - R)$ of this production that is

associated with external inputs of N, both of which we already have from the N-cycle model of Ref. S2,

$$P_{O2} = \left(\frac{x + \frac{1}{4}z + 2y}{x}\right) \cdot \left(\frac{x}{y}\right) \cdot P_{Norg} - \frac{5}{4}(1 - R) \cdot P_{Norg}$$

$$= \left(\frac{x+\frac{1}{4}z}{x}\right) \cdot \left(\frac{x}{y}\right) \cdot P_{Norg} + 2P_{Norg} - \frac{5}{4}(1 - R) \cdot P_{Norg} \quad \text{(S12)}$$

$$= r_{-\mathrm{O2:C}} \cdot r_{\mathrm{C:N}} \cdot P_{Norg} + 2(1 - R + R)P_{Norg} - \frac{5}{4}(1 - R) \cdot P_{Norg}$$

$$= P_{COD} + 2RP_{Norg} - \frac{3}{4}(1 - R) \cdot P_{Norg}$$

where

$$r_{-\mathrm{O2:C}} \equiv 1 + \frac{1}{4}\frac{z}{x},$$

$$r_{\mathrm{C:N}} \equiv \frac{x}{y}, \text{ and} \quad \text{(S13)}$$

$$P_{COD} \equiv r_{-\mathrm{O2:C}}\, r_{\mathrm{C:N}} \cdot P_{Norg}.$$

P_{COD} is the production rate of chemical oxygen demand associated with the oxidative state of the organic C alone. The chemical oxygen demand associated with the oxidative state of the organic N is tracked separately. In other words, P_{COD} is almost equivalent to the rate of organic carbon production except that COD unlike $\mathrm{C_{org}}$, keeps track of the oxidative state of the carbon in such a way that by definition the respiration of one mole of COD consumes exactly one mole of $\mathrm{O_2}$.

<u>The loss of $\mathrm{O_2}$ due to respiration:</u> To compute the loss of $\mathrm{O_2}$ associated with the respiration of organic matter we consider the following two reactions

$$\mathrm{DOD} + \mathrm{O_2} \rightarrow \mathrm{CO_2}, \quad \text{(S14)}$$

$$\mathrm{DOD} + 2\,\mathrm{O_2} \rightarrow \mathrm{NO_3^-}$$

where the DOD is the dissolved phase of the chemical oxygen demand tracer and DON is the dissolved phase of the organic nitrogen tracer. Where the oxygen concentration is low either in the water column or in benthic sediments, $\mathrm{NO_3^-}$ rather than $\mathrm{O_2}$ is the dominant oxidant for the consumption of DOD:

$$\mathrm{DOD} + \tfrac{5}{4}\mathrm{NO_3^-} \rightarrow \mathrm{CO_2}. \tag{S15}$$

The rate of oxygen utilization associated with the loss of DOD must therefore decrease by 5/4 times the rate of water-column and benthic denitrification. Thus, the net rate of oxygen utilization associated with the respiration of organic matter is given by

$$L_{O2} = \kappa_{dC}[\mathrm{DOD}] + 2\kappa_{dN}[\mathrm{DON}] - \tfrac{5}{4}(D_{wc} + D_{sed}), \tag{S16}$$

Where D_{wc} and D_{sed} are the water-column and benthic denitrification rates, which are available from the N-cycle model of Ref. S2.

The governing equation for the oxygen demand tracers: We treat the concentrations of DOC, DON, and DOD as independent dissolved tracers and the concentrations of POC, PON, and POD as independent sinking-particulate-matter tracers. This simplification is required in order to avoid having to carry a full spectrum of organic compounds that are presently uncharacterized with unknown production rates and with unknown carbon and nitrogen oxidative states.

For the inverse model, we define the stoichiometric ratio, $r_{-\mathrm{O2:C}}$, for the exported organic matter based on the location of production rather than on the location of respiration. This distinction is important because, we do not have to assume that DOC, DON, and DOD are produced or respired at the same rate everywhere in the ocean. We thus track the oxidative demand for carbon and nitrogen separately. The model can therefore allow the $\mathrm{C{:}N}$ and $-\mathrm{O_2{:}C}$ stoichiometric ratios to vary independently as a function of surface location where the organic matter is produced.

The movement of the CODtracers: The production of COD is routed into two pools: DOD and POD. DOD is a dissolved phase that is transported by fluid motion and is respired at a constant rate κ_{dC}. POD is a sinking particulate phase that is transported downwards by gravitational settling and solubilized into DOD at a constant rate κ_P. Their governing equations are

$$\left[\frac{d}{dt} + \mathbf{T}\right][\mathrm{DOD}] = \sigma P_{COD} + \kappa_P[\mathrm{POD}] - \kappa_{dC}[\mathrm{DOD}], \tag{S17}$$

$$\left[\frac{d}{dt} + \mathbf{F}_{POD}\right][\mathrm{POD}] = (1-\sigma)P_{COD} - \kappa_P[\mathrm{POD}],$$

where $\mathbf{F}_{POD}$ is the flux-divergence operator for sinking particulate organic matter, i.e.

$$\mathbf{F}_{POD}\mathrm{c} = \frac{\partial}{\partial z}\left(w_s \frac{\partial c}{\partial z}\right). \tag{S18}$$

The sinking speed w_s is chosen to produce a power-law flux-attenuation profile with exponent b_o. A fraction σ of the COD production is directly allocated to the dissolved phase with the remaining fraction, $1-\sigma$, is allocated to the sinking particulate phase.

As previously noted in equation S13 the production of COD is taken to be proportional to the rate of organic carbon production with a proportionality constant modeled as either a linear function of sea surface temperature (SST) or of the surface nitrate concentration (SSN),

$$r_{-\mathrm{O2:C}} = mz + b, \tag{S19}$$

where z can be either z_{A} or z_{B} as defined in equations S2 and S3 and where m and b are adjustable parameters to be estimated form the data as part of the inversion process. Thus, the steady-state $[\mathrm{COD}]$ distribution is given by the solution to the following linear system of equations

$$\begin{bmatrix} \mathbf{T} + \kappa_{dC}\mathbf{I} & -\kappa_{dC}\mathbf{I} \\ \mathbf{0} & \mathbf{F}_{POD} + \kappa_P\mathbf{I} \end{bmatrix} \begin{bmatrix} [\mathrm{DOD}] \\ [\mathrm{POD}] \end{bmatrix} = \begin{bmatrix} \sigma\mathbf{I} \\ (1-\sigma)\mathbf{I} \end{bmatrix} P_{COD}, \tag{S20}$$

with

$$P_{COD} = r_{\mathrm{C:N}}\,[\mathbf{diag}\,(P_{Norg})][z \quad \mathbf{1}]\begin{bmatrix} m \\ b \end{bmatrix}. \tag{S21}$$

The governing equations for organic carbon: The governing equations for organic carbon are given by

$$\left[\frac{d}{dt}+\mathbf{T}\right][\mathrm{DOC}] = \sigma r_{\mathrm{C:N}} P_{Norg} + \kappa_P[\mathrm{POC}] - \kappa_{dC}[\mathrm{DOC}]\,, \tag{S22}$$

$$\left[\frac{d}{dt}+\mathbf{F}_{POC}\right][\mathrm{POC}] = (1-\sigma) r_{\mathrm{C:N}} P_{Norg} - \kappa_P[\mathrm{POC}].$$

The sinking particulate flux divergence operator, $\boldsymbol{F}_{POC}$ is constructed to produce a power-law flux attenuation profile with exponent b_c. By separating the remineralization depth profiles of carbon and oxygen ($b_c$and b_o), we account for the possibility that the oxidative state of exported organic matter changes as a function of depth and a depth dependent $r_{-\mathrm{O2:C}}$. The steady-state organic carbon distribution is given by the solution to the following linear system of equations

$$\begin{bmatrix}\mathbf{T}+\kappa_{dC}\mathbf{I} & -\kappa_P\mathbf{I} \\ \mathbf{0} & \mathbf{F}_{POC}+\kappa_P\mathbf{I}\end{bmatrix}\begin{bmatrix}[\mathrm{DOC}] \\ [\mathrm{POC}]\end{bmatrix} = r_{\mathrm{C:N}}\begin{bmatrix}\sigma\mathbf{I} \\ (1-\sigma)\mathbf{I}\end{bmatrix} P_{Norg}. \tag{S23}$$

The governing equation for inorganic carbon: The governing equation for inorganic carbon (DIC) is given by:

$$\left[\frac{d}{dt}+\mathbf{T}\right][\mathrm{DIC}] = -r_{\mathrm{C:N}} P_{\mathrm{Norg}} - r_{\mathrm{PIC:Corg}} r_{\mathrm{C:N}} P_{\mathrm{Norg}} + \kappa_{\mathrm{PIC}}[\mathrm{PIC}] + \kappa_{dC}[\mathrm{DOC}]$$

$$+\mathbf{K}_{CO2}([\mathrm{CO_2}]_{\mathrm{sat}} - [\mathrm{CO_2}]_{\mathrm{surf}}), \tag{S24}$$

$$\left[\frac{d}{dt}+\mathbf{F}_{PIC}\right][\mathrm{PIC}] = r_{\mathrm{PIC:Corg}} r_{\mathrm{C:N}} P_{Norg} - \kappa_{\mathrm{PIC}}[\mathrm{PIC}],$$

where $\mathbf{K}_{CO2}$ is the air-sea gas exchange operator, $[\mathrm{CO_2}]_{\mathrm{sat}} = \alpha_C p\mathrm{CO}_{2,\mathrm{atm}} P/P_0$ is the concentration of $\mathrm{CO_2}$ in surface waters, $[\mathrm{CO_2}]_{\mathrm{sat}}$ is the surface aqueous $\mathrm{CO_2}$ concentration, which is computed from $[\mathrm{DIC}]$ using CO2SYS [Ref. S4, S5]. The alkalinity, temperature, salinity, silicic acid, and phosphate concentrations needed to evaluate the equilibrium constants are obtained from observations interpolated to the model grid. We use the OCMIP-2 air-sea gas exchange formulation (http://ocmip5.ipsl.jussieu.fr/OCMIP/phase2/simulations/).

Anthropogenic carbon: Because $p\mathrm{CO}_{2,\mathrm{atm}}$ has been increasing rapidly in response to anthropogenic perturbations to the carbon cycle we need to account for the additional carbon in the ocean that is not in steady state. We assume that the marine DIC concentration can be decomposed into an anthropogenic part, $\mathrm{DIC}_{\mathrm{ant}}$, and a natural part that is assumed to be in a climatological steady state. We compute the natural DIC concentration by solving the following steady state system using Newton's method

$$\begin{aligned}\mathbf{T}[\mathrm{DIC}]_{\mathrm{nat}} = & -r_{\mathrm{C:N}}P_{\mathrm{Norg}} - r_{\mathrm{PIC:Corg}} \pm r_{\mathrm{C:N}}P_{N\mathrm{org}} + \kappa_{\mathrm{PIC}}[\mathrm{PIC}]_{\mathrm{nat}} + \kappa_{dC}[\mathrm{DOC}] \\ & + \mathbf{K}_{CO2}\left([\mathrm{CO}_2]_{\mathrm{sat}} - [\mathrm{CO}_2]_{\mathrm{surf}}\right), \qquad \text{(S25)} \\ \mathbf{F}_{\mathrm{PIC}}[\mathrm{PIC}]_{\mathrm{nat}} = & \; r_{\mathrm{PIC:Corg}}r_{\mathrm{C:N}}P_{N\mathrm{org}} - \kappa_{\mathrm{PIC}}[\mathrm{PIC}]_{\mathrm{nat}},\end{aligned}$$

in which $[\mathrm{CO}_2]_{\mathrm{sat}}$ corresponds to the saturation concentration assuming a preindustrial ($t = 1765$) atmospheric CO_2 partial pressure of 278 ppm. We then compute $\mathrm{DIC}_{\mathrm{ant}}$ from

$$\mathrm{DIC}_{\mathrm{ant}} \equiv \mathrm{DIC}(2013) - \mathrm{DIC}_{\mathrm{nat}}, \qquad \text{(S26)}$$

with $\mathrm{DIC}(2013)$ obtained by solving the transient problem from $t = 1765$ to $t = 2013$ subject to the initial condition $\mathrm{DIC}(1765) = \mathrm{DIC}_{\mathrm{nat}}$and $\mathrm{PIC}(1765) = \mathrm{PIC}_{\mathrm{nat}}$ and with $[\mathrm{CO}_2]_{\mathrm{sat}}(t)$ prescribed using the observed atmospheric $p\mathrm{CO}_2$ history. We then add back a fixed $\mathrm{DIC}_{\mathrm{ant}}$ to the $\mathrm{DIC}_{\mathrm{nat}}$, which is an implicit function of the model parameters, to get the total DIC concentration. The difference between the total DIC and the observed DIC is then used to construct the likelihood function.

The data: The $[\mathrm{O}_2]$ and $[\mathrm{DIC}]$ measurements used to constrain the model are form the GLODAPv2 database (Ref. S6) and the $[\mathrm{DOC}]$ measurements are from Ref. S7. After bin-averaging the hydrographic bottle measurements to the model grid we have $n_{\mathrm{O2}} = 84{,}207$, $n_{\mathrm{DIC}} = 66{,}964$, and $n_{\mathrm{DOC}} = 13{,}148$ independent data points. We combine these data into an $n_{\mathrm{obs}}\times 1$ vector

$$\mathrm{d}_{obs} = \begin{bmatrix}[\mathrm{O}_2]_{\mathrm{obs}} \\ [\mathrm{DIC}]_{\mathrm{obs}} \\ [\mathrm{DOC}]_{\mathrm{obs}}\end{bmatrix} \qquad \text{(S27)}$$

with $\mathrm{n_{obs}} = n_{\mathrm{O2}} + n_{\mathrm{DIC}} + n_{\mathrm{DOC}}$.

The probability model: To estimate $r_{-\mathrm{O2:C}}$ we assign a multivariate normal probability model to $\mathbf{d}_{\mathrm{obs}}$. We take the mean of this probability model to be given by the solution of our forward biogeochemical model. The probability of $\mathbf{d}_{\mathrm{obs}}$ is thus conditioned on *m*, *b*, and the 4 additional nuisance parameters, b_c, b_o, κ_{dC}, and σ, through their influence on the solution of the biogeochemical model. Denoting the vector of model parameters by β, the probability of $\mathbf{d}_{\mathrm{obs}}$ given (a.k.a. the likelihood function) is given by

$$\mathrm{prob}(\mathbf{d}_{\mathrm{obs}}|\beta,\alpha) = (\tfrac{\alpha}{2\pi})^{\frac{n_{obs}}{2}} \det(\mathbf{W})^{\frac{1}{2}} \exp\{-\alpha\mathcal{L}(\beta)\}, \tag{S28}$$

where

$$\mathcal{L}(\beta) \equiv \tfrac{1}{2}\big(\mathbf{d}_{\mathrm{obs}} - \mathbf{d}(\beta)\big)'\mathbf{W}\big(\mathbf{d}_{\mathrm{obs}} - \mathbf{d}(\beta)\big). \tag{S29}$$

with

$$\mu(\beta) = \mathbf{H}\begin{bmatrix}[\mathrm{O_2}]\\ [\mathrm{DIC}]\\ [\mathrm{DOC}]\end{bmatrix}, \tag{S30}$$

is the solution to the forward biogeochemical model evaluated at the grid-boxes with observations. The block-diagonal matrix,

$$\mathbf{H} = \begin{bmatrix}\mathbf{H'_{O2}} & \mathbf{0} & \mathbf{0}\\ \mathbf{0} & \mathbf{H'_{DIC}} & \mathbf{0}\\ \mathbf{0} & \mathbf{0} & \mathbf{H'_{DOC}}\end{bmatrix}, \tag{S31}$$

selects those grid-boxes for which observations are available in the database, i.e. $\mathbf{H}_{\mathrm{O2}}$, $\mathbf{H}_{\mathrm{DIC}}$, and $\mathbf{H}_{\mathrm{DOC}}$ are $n_{\mathrm{O2}} \times n_{\mathrm{mod}}$, $n_{\mathrm{DIC}} \times n_{\mathrm{mod}}$, and $n_{\mathrm{DOC}} \times n_{\mathrm{mod}}$ matrices that extract only the grid-boxes that have at least one observation of $[\mathrm{O_2}]$, $[\mathrm{DIC}]$, and $[\mathrm{DOC}]$ respectively. The primes are used to denote the matrix transpose operation. We assume that the bin-averaged observations are independent so that the precision matrix in the multivariate normal model is given by a diagonal matrix,

$$\alpha\mathbf{W} = \alpha\mathbf{H} = \begin{bmatrix}\mathbf{V}/\sigma^2_{\mathrm{O2}} & \mathbf{0} & \mathbf{0}\\ \mathbf{0} & \mathbf{V}/\sigma^2_{\mathrm{DIC}} & \mathbf{0}\\ \mathbf{0} & \mathbf{0} & \mathbf{V}/\sigma^2_{\mathrm{DOC}}\end{bmatrix}\mathbf{H}'. \tag{S32}$$

The parameter that scale the precision matrix is an unknown parameter that needs to be estimated as part of the Bayesian inversion. The parameters σ_{O2}^2, σ_{DIC}^2, and σ_{DOC}^2 are the spatial variances of the tracer observations computed as follows

$$\sigma_{O2}^2 = \frac{([O_2]_{obs} - \mu_{O2})' \mathbf{H}_{O2} \mathbf{V} \mathbf{H}'_{O2} ([O_2]_{obs} - \mu_{O2})}{\mathbf{1}' \mathbf{H}_{O2} \mathbf{V} \mathbf{H}'_{O2} \mathbf{1}},$$

$$\sigma_{DIC}^2 = \frac{([DIC]_{obs} - \mu_{DIC})' \mathbf{H}_{DIC} \mathbf{V} \mathbf{H}'_{DIC} ([DIC]_{obs} - \mu_{DIC})}{\mathbf{1}' \mathbf{H}_{DIC} \mathbf{V} \mathbf{H}'_{DIC} \mathbf{1}}, \quad \text{(S33)}$$

$$\sigma_{DOC}^2 = \frac{([DOC]_{obs} - \mu_{DOC})' \mathbf{H}_{DOC} \mathbf{V} \mathbf{H}'_{DOC} ([DOC]_{obs} - \mu_{DOC})}{\mathbf{1}' \mathbf{H}_{DOC} \mathbf{V} \mathbf{H}'_{DOC} \mathbf{1}},$$

with

$$\mu_{O_2} = \frac{\mathbf{1}' \mathbf{H}_{O_2} \mathbf{V} \mathbf{H}'_{O2} [O_2]_{obs}}{\mathbf{1}' \mathbf{H}_{O2} \mathbf{V} \mathbf{H}'_{O2} \mathbf{1}},$$

$$\mu_{DIC} = \frac{\mathbf{1}' \mathbf{H}_{DIC} \mathbf{V} \mathbf{H}'_{O_2} [DIC]_{obs}}{\mathbf{1}' \mathbf{H}_{DIC} \mathbf{V} \mathbf{H}'_{DIC} \mathbf{1}}, \quad \text{(S34)}$$

$$\mu_{DOC} = \frac{\mathbf{1}' \mathbf{H}_{DOC} \mathbf{V} \mathbf{H}'_{DOC} [DOC]_{obs}}{\mathbf{1}' \mathbf{H}_{DOC} \mathbf{V} \mathbf{H}'_{DOC} \mathbf{1}}.$$

In the above expressions, $\mathbf{V}$ is the diagonal matrix formed from a vector whose elements are the fraction of the total ocean volume in each of the circulation model's grid-boxes, the bold $\mathbf{1}$'s are appropriately-sized column vectors of ones.

2. Parameter estimation:

As formulated, the model predicts the three-dimensional distributions of DIC, DOC, and $[O_2]$ using 6 adjustable parameters m, b, σ, κ_{dC}, b_c, and b_o. We fix the C:N ratio to $r_{C:N} = 106/16$.

To estimate the adjustable parameters we assign a flat prior probability to

$$\beta = [m \quad b \quad \log\sigma \quad \log\kappa_{dC} \quad \log b_c \quad \log b_o]'. \quad \text{(S35)}$$

and then use Laplace's method to obtain a normal approximation to the posterior, i.e.

$$\text{prob}(\beta, \alpha | \boldsymbol{d}_{obs}) \approx |\det \Sigma|^{-1/2} \exp\left\{-\frac{1}{2}(\beta - \hat{\beta})' \Sigma^{-1} (\beta - \hat{\beta})\right\}, \quad \text{(S36)}$$

where the posterior parameter covariance matrix is given by

$$\Sigma = [\hat{\alpha} \nabla_\beta \nabla_\beta \mathcal{L}(\beta)|_{\beta=\hat{\beta}}]^{-1}, \quad \text{(S37)}$$

with

$$\hat{\beta} = \underset{\beta}{\operatorname{argmin}}\, \mathcal{L}(\beta). \tag{S38}$$

The parameter $\hat{\alpha}$ that scales the posterior parameter precision matrix is chosen to be the value that maximizes the posterior probability distribution, i.e.

$$\hat{\alpha} = \frac{n_{obs}}{2\mathcal{L}(\hat{\beta})}. \tag{S39}$$

The posterior parameter estimates: The optimal model parameters along with their posterior error bars for the model in which $r_{-\mathrm{O2:C}}$ is parameterized in terms of SST are

$$\widehat{\beta_A} = \begin{bmatrix} \widehat{m} \\ \widehat{b} \\ \widehat{\log \kappa_{dC}} \\ \widehat{\log \sigma} \\ \widehat{\log b_C} \\ \widehat{\log b_O} \end{bmatrix} = \begin{bmatrix} (1.6184 \pm 0.0339) \times 10^{-2} (^{\circ}\mathrm{C})^{-1} \\ 0.7312 \pm 0.0048 \\ -17.3403 \pm 0.0033 \\ -1.5178 \pm 0.0200 \\ 0.1267 \pm 0.0033 \\ 0.0231 \pm 0.0018 \end{bmatrix}. \tag{S40}$$

The positive slope, *m* implies that the oxygen demand for the respiration of organic matter produced in warmer waters is higher than the oxygen demand for the respiration of organic matter produced in colder waters.

For the model in which $r_{-\mathrm{O2:C}}$ is parameterized in terms of SSN the optimal parameter values are

$$\widehat{\beta_A} = \begin{bmatrix} \widehat{m} \\ \widehat{b} \\ \widehat{\log \kappa_{dC}} \\ \widehat{\log \sigma} \\ \widehat{\log b_C} \\ \widehat{\log b_O} \end{bmatrix} = \begin{bmatrix} (-6.949 \pm 0.477) \times 10^{-3} (\mathrm{mmol/m^3})^{-1} \\ 1.0114 \pm 0.0043 \\ -17.3465 \pm 0.0033 \\ -1.8336 \pm 0.0315 \\ 0.1675 \pm 0.0030 \\ 0.0515 \pm 0.0019 \end{bmatrix}. \tag{S41}$$

In this case we find a negative slope, m, implying that oxygen demand for the respiration of organic matter produced in low-nutrient environments is higher than when produced in high-nutrient environment. Given the negative correlation between SST and surface nutrient concentrations, the signs of the slope are consistent.

The most probably parameter values (not log transformed) and their 95% probability intervals are given in Tables S6. For both models, the exponent for the POC flux attenuation profile is approximately 10% larger than the exponent for POD. This suggests that the amount of oxygen needed to respire a mole of organic carbon tends to increase with depth and an overall

decrease in organic carbon oxidation state. However, the probability intervals for these exponents largely overlap indicating that the hydrographic data combined with our inverse model does not provide enough information to robustly identify any depth variation in $r_{-\mathrm{O2:C}}$.

The residual misfits for the temperature-dependent and nitrate-dependent $r_{-\mathrm{O2:C}}$ models differ by less than 1%, with the SST model producing the smaller residual error,

$$\frac{\mathcal{L}_A(\widehat{\beta_A})}{\mathcal{L}_B(\widehat{\beta_B})} = 0.9930. \tag{S42}$$

The number of observations used to constrain the model is large, $n_{obs} = 164{,}319$ resulting in a significant difference and a larger posterior probability for model A compared to model B. If we assign an equal prior probability to model A and B as well as the same flat prior probability density for the parameters for both models and use Laplace's approximation to marginalize out β, the posterior odds in favor of model A compared to model B [e.g. Ref. S8], simplifies to

$$\begin{aligned}\frac{prob\ (\text{model A}|d_{obs})}{prob\ (\text{model B}|d_{obs})} &\approx \frac{prob\ (d_{obs}|\widehat{\beta_A}, \widehat{\alpha_A}, \text{model A}\ )}{prob\ (d_{obs}|\widehat{\beta_B}, \widehat{\alpha_B},\ \text{model B})} \times \frac{\sqrt{\det \Sigma_A}}{\sqrt{\det \Sigma_B}} \\ &= \left(\frac{\mathcal{L}_A(\widehat{\beta_A})}{\mathcal{L}_B(\widehat{\beta_B})}\right)^{-\frac{(n_{obs}-6)}{2}} \times \left[\frac{\det[\nabla_\beta \nabla_\beta \mathcal{L}_A(\beta)|_{\beta=\widehat{\beta_A}}]}{\det[\nabla_\beta \nabla_\beta \mathcal{L}_B(\beta)|_{\beta=\widehat{\beta_B}}]}\right]^{-1/2}, \\ &\approx 10^{250}.\end{aligned} \tag{S43}$$

This astronomically large preference for model A depends crucially on the assumption that all n_{obs} residuals are independent, which is unlikely to be the case. But even if we assume that only one out of every 100 data point provides an independent degree of freedom, the odds in favor of model A compared to model B would still be greater than $10^2{:}\,1$.

It is useful to compare the correlation matrix for the posterior probability distribution of the parameters (Table S7). The magnitude of correlation between m and the other parameters is generally larger for model A. This makes the temperature-dependent model (model A) a bit more fragile in the sense that a change in the value of m will necessitate a recalibration of the other model parameters to avoid a large degradation model fit quality. The smaller parameter correlations in model B implies a model that is somewhat less inter-dependent. However, because each model has only 6 adjustable parameters, the penalty against model A in the

expression for the posterior odds given in (S43) is less than a factor of 10. This factor is insignificant compared to the penalty against model B due to its poorer fit to the observations.

Globally Integrated oxygen consumption and carbon respiration rates: The volume integrated oxygen consumption and carbon respiration rates for the models A and B are given in Table S8. Figure S8 plots the carbon production partitioned according to the value of $r_{-\mathrm{O2:C}}$ used to determine the chemical oxygen demand of the exported organic carbon to the COD tracer for each model. The carbon-export weighted mean $r_{-\mathrm{O2:C}}$ for model A is 0.9491 and for model B is 0.9577.

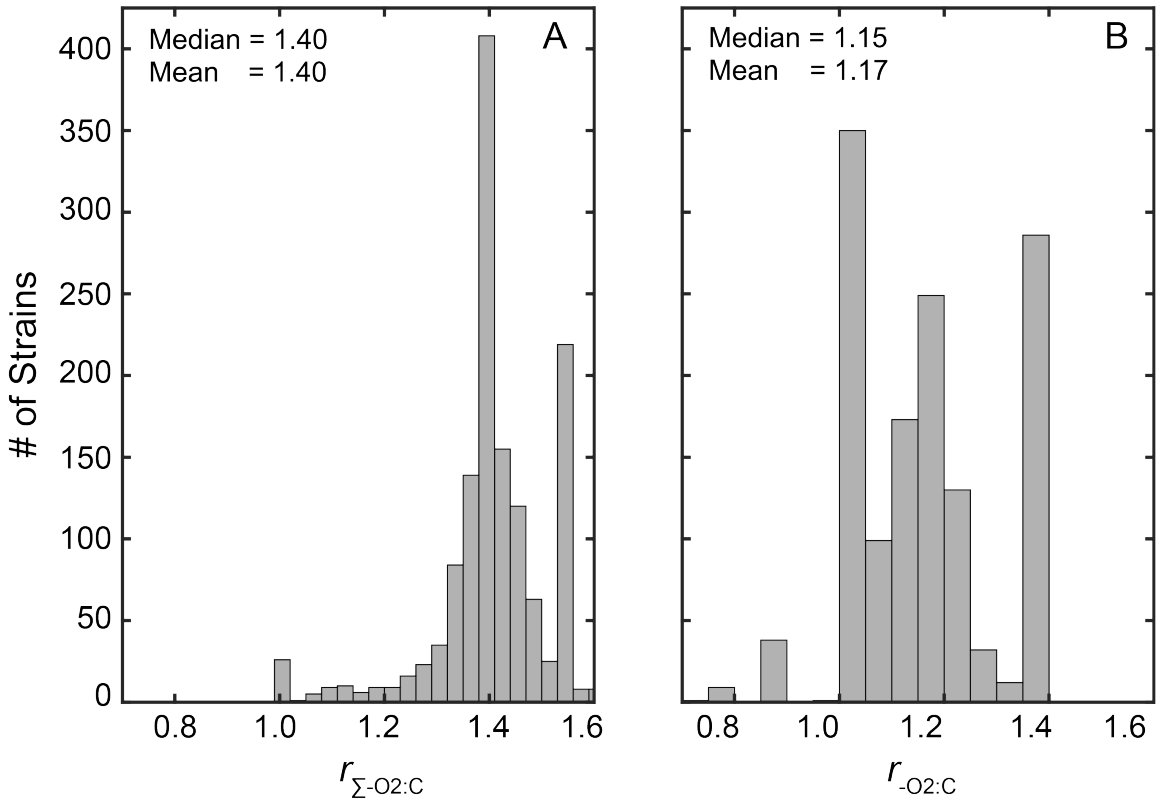

Fig. S1. Predicted distribution of the respiration quotient across microalgae species. A. The total respiration quotient ($r_{\Sigma-O2:C}$) and B. The respiration quotient ($r_{-O2:C}$). The predictions are based on the biochemical composition of 1562 phytoplankton cultures (Ref. S9).

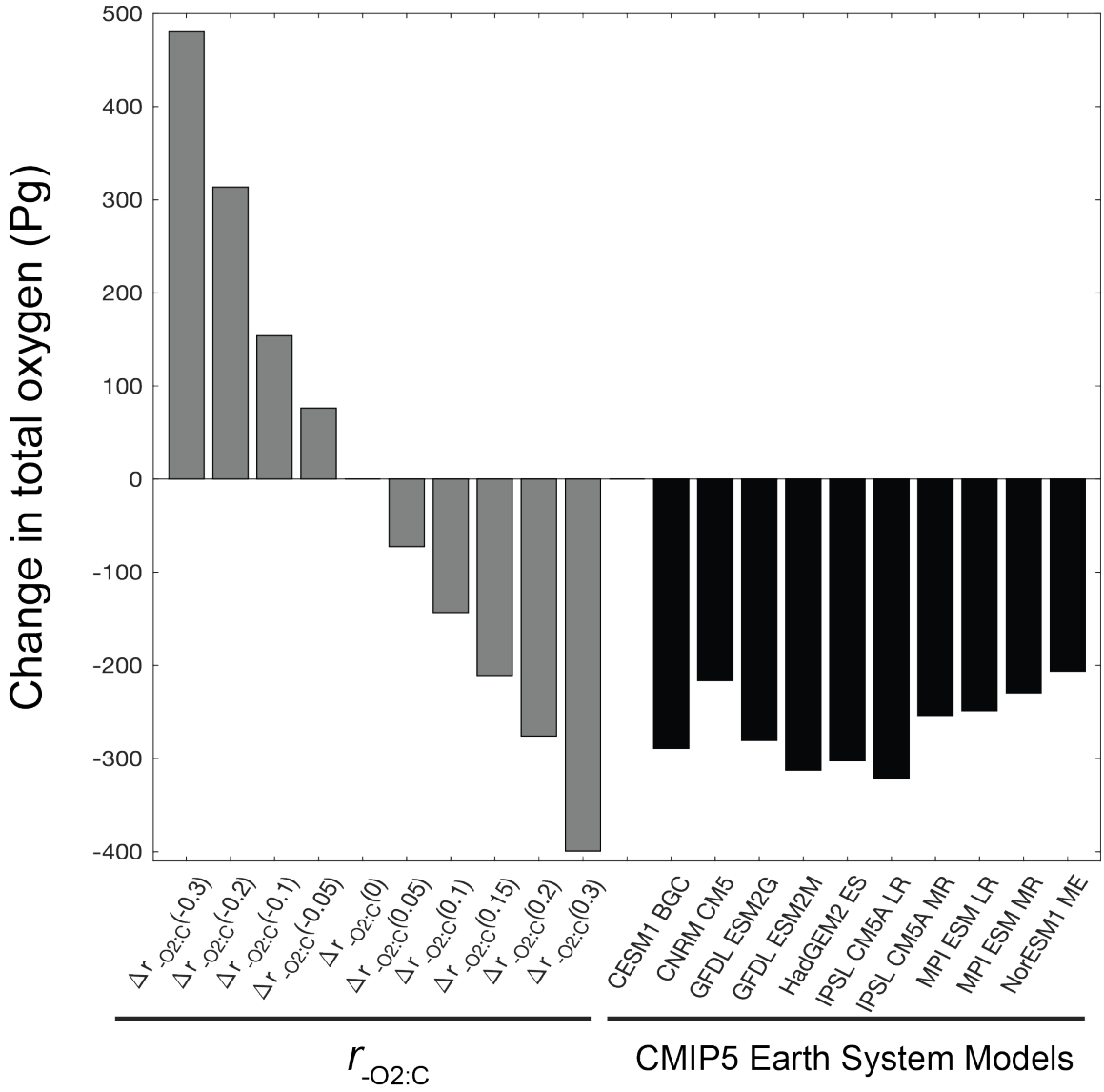

Fig. S2. Comparison of changes to oxygen levels via changes to the respiration quotient or climate change. Changes in global marine oxygen levels by a changing respiration quotient (*in grey*) after 300 yrs and 2100 under the climate change scenario RCP8.5 (*in black*). The climate model outputs are from CMIP5.

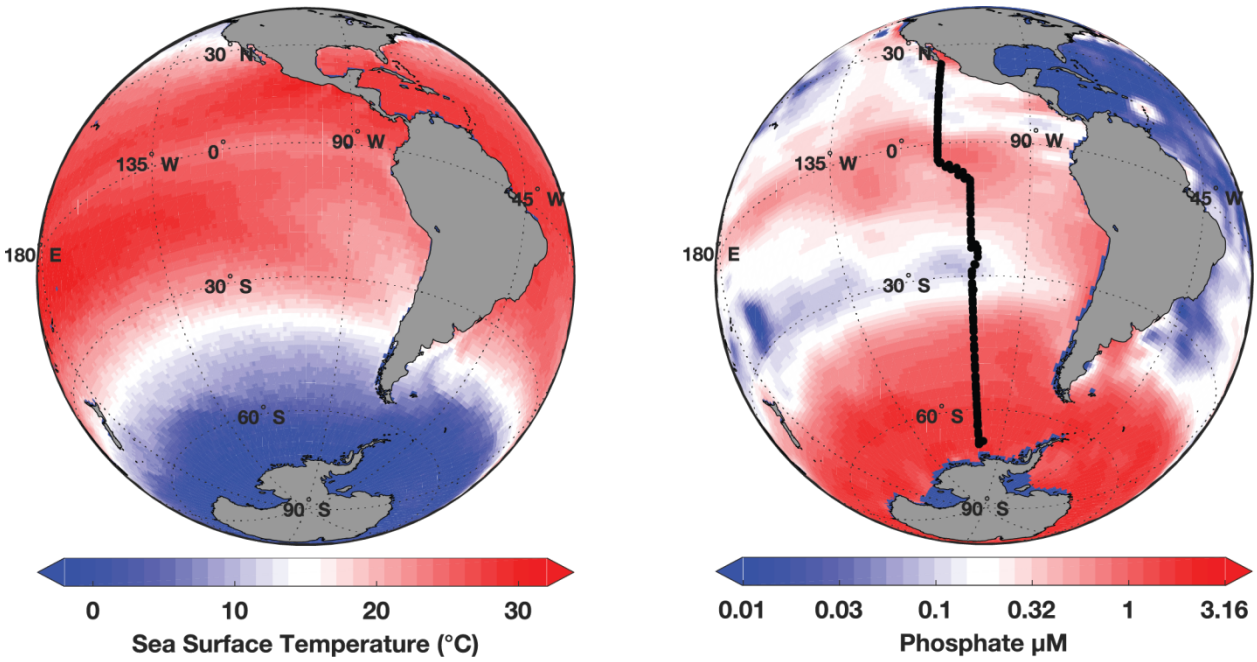

Fig. S3. P18 GO-SHIP Cruise track locations from San Diego, CA (32.72° N, 117.16°W) to Antarctica (77.85°S, 166.67°E). Background phosphate concentrations are from the GLODAPv2 database (Ref. S6).

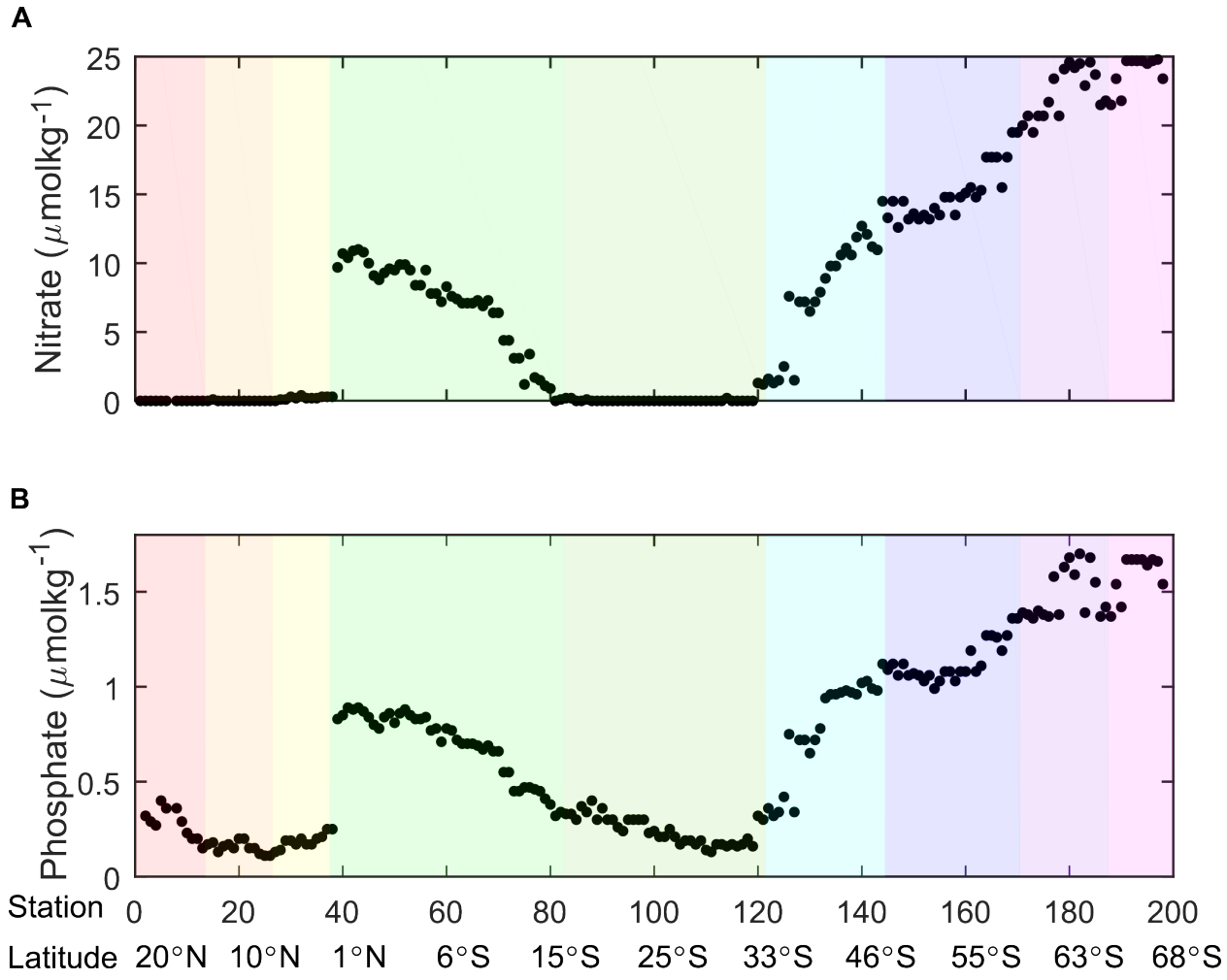

Fig. S4. Observed nitrate (a) and phosphate (b) concentrations across the P18 cruise track. Colored background represents each ocean biome region.

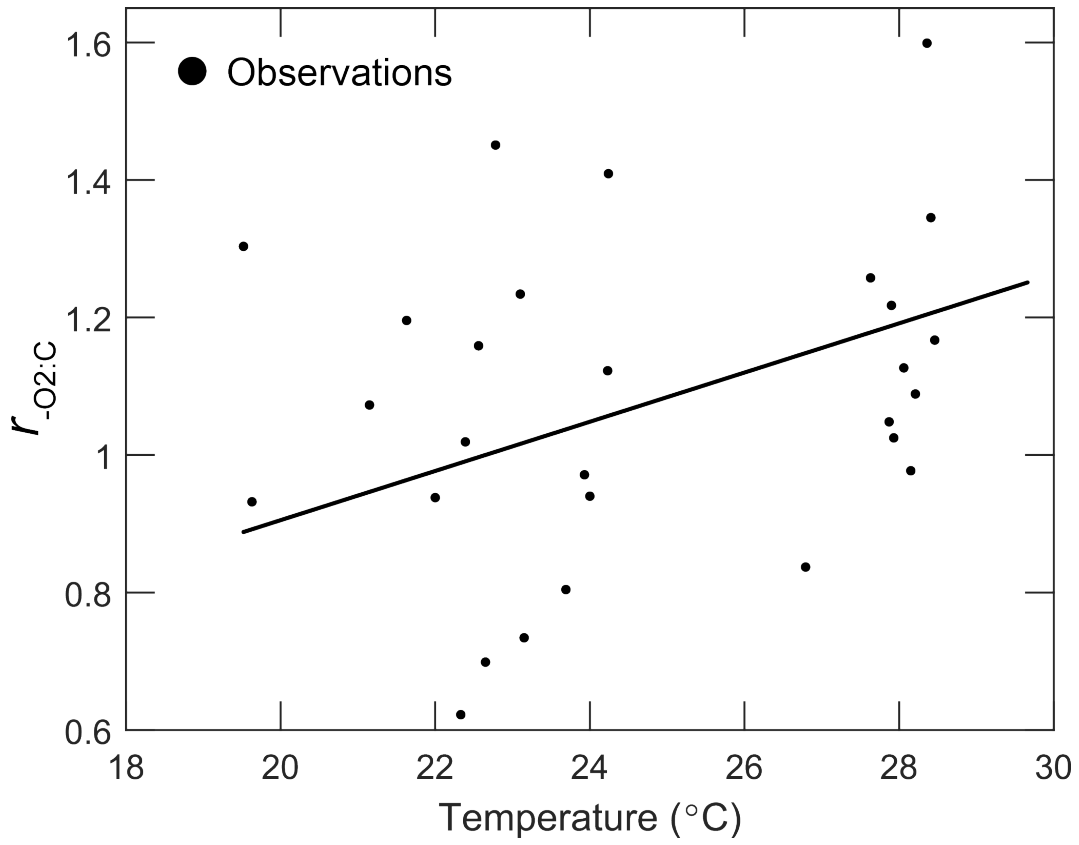

Fig. S5. Relationship between temperature and the respiration quotient derived from a CHNOPS elemental analysis of marine POM from the Western North Pacific Ocean (Ref. S10). The line represents a linear fitted model of temperature and $r_{-O2:C}$ ($r_{-O2:C}$ = 0.19 + (0.036/℃)**SST*; p-value = 0.05).

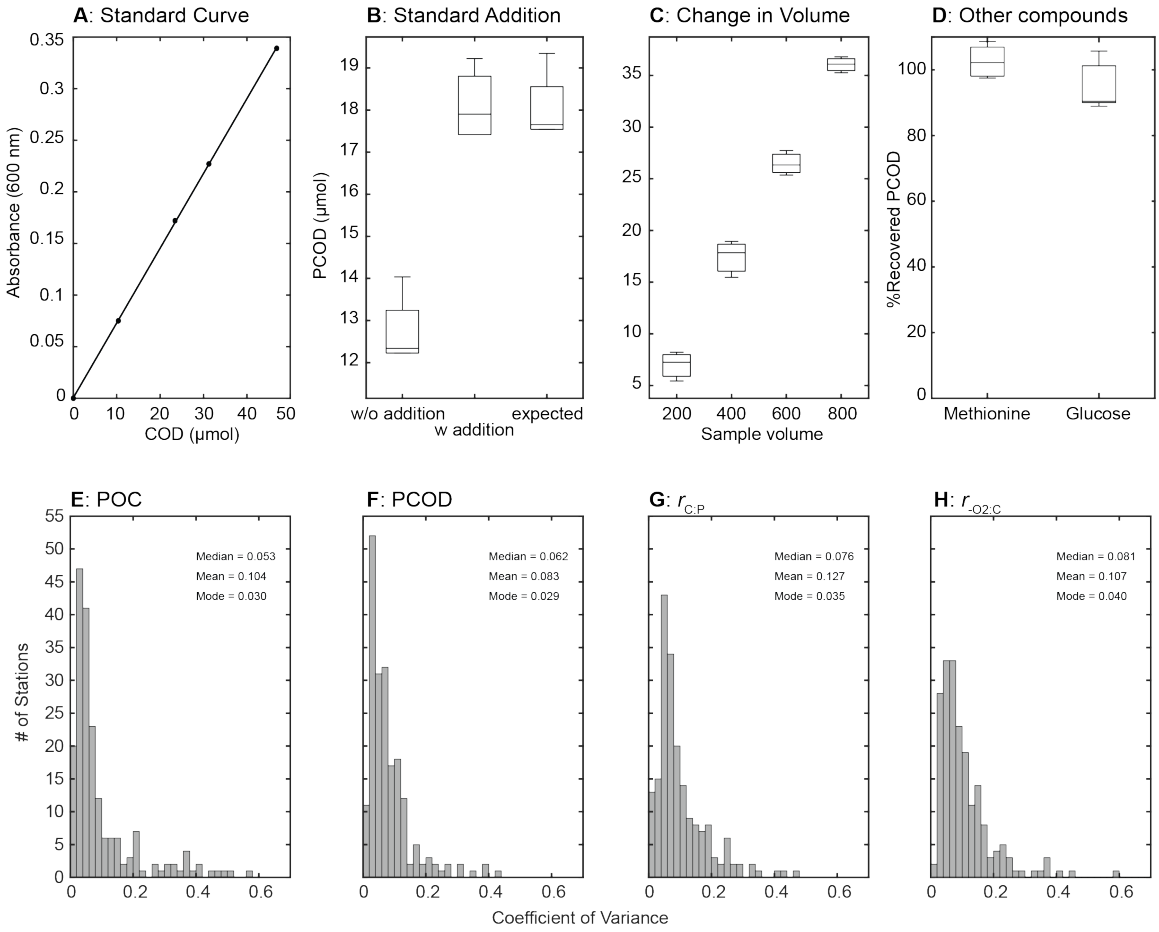

Fig. S6. Optimization and evaluation of a method for quantifying the oxygen demand of marine POM. A: PCOD standard curve using a Hach-certified phthalate standard curve. B: Recovery of the PCOD after experimentally adding organic material to a seawater sample. C: Relationship between sample volume and measured PCOD. D: Testing Two Organic Compounds (Methionine (Met), Glutamic acid (Glu)), averaged on their expected values using phthalate standard. Coefficient of variance in E: [POC], F: [PCOD], G: $r_{C:P}$, and H: The respiration quotient.

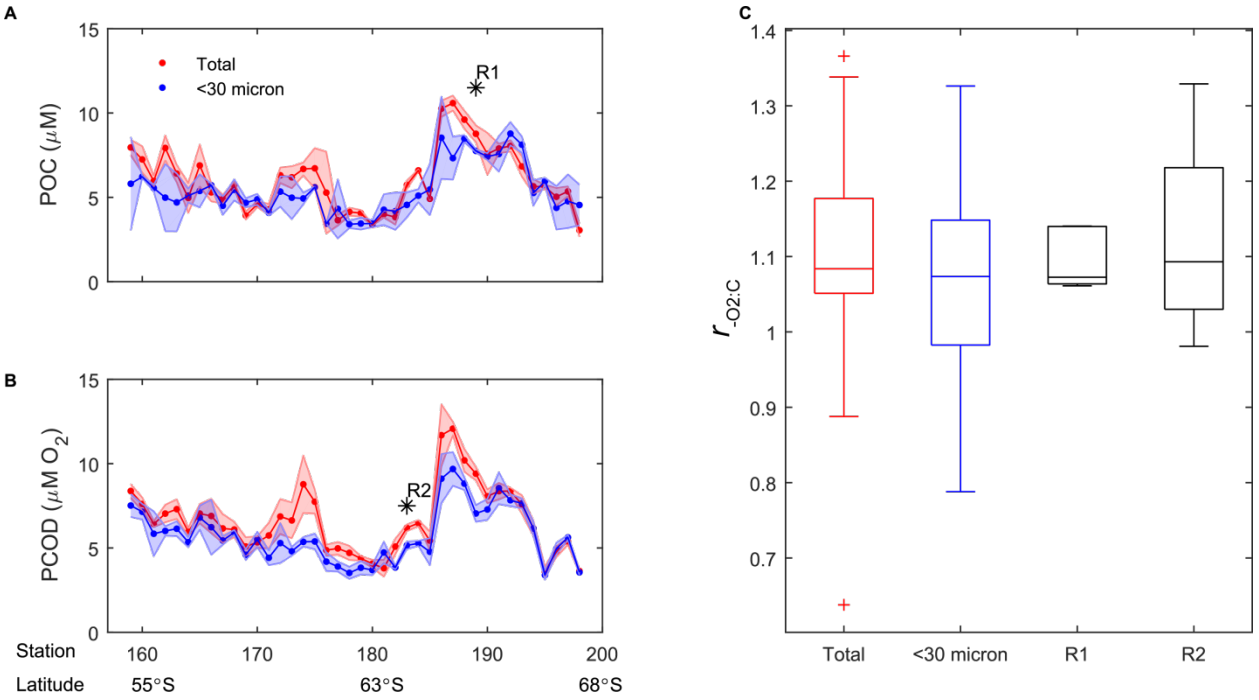

Fig. S7. Comparison of PCOD concentrations in different size fractions. A. Particulate organic carbon in samples <30 µm and with no size-fractionation. B: Particulate chemical oxygen demand in samples <30 µm and with no size-fractionation. C: The respiration quotient for <30 µm and total samples as well as for two regions with significant POM concentration differences (R1 and R2).

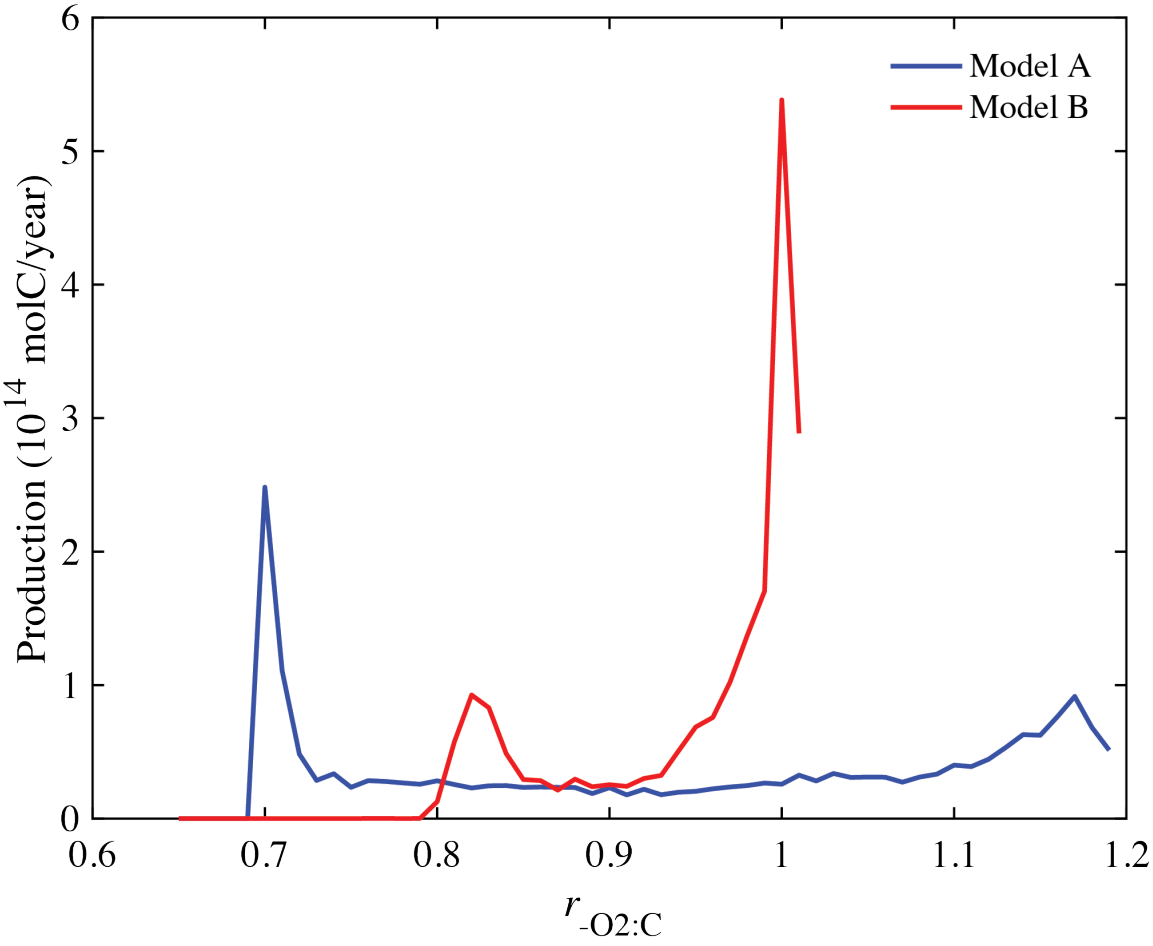

Fig. S8. Carbon production partitioned according to the $r_{-O2:C}$ value used to determine the chemical oxygen demand of the exported organic carbon (Model A: $r_{-O2:C}$ ~ SST, Model B: $r_{-O2:C}$ ~ [Nitrate]) .

Table S1.
Model change in oxygen levels.

ESM Model	Ocean module	Depth layers	O_2 (Pg)	Resolution	Reference
CESM1-BGC	BEC	60	-289	1.125˚/0.27˚-0.53˚	S11
GFDL-ESM2G	TOPAZ2	63	-281	0.3–1˚	S12
GFDL-ESM2M	TOPAZ2	50	-312	0.3–1˚	S12
HadGEM2-ES	Diat-HadOCC	40	-303	0.3–1˚	S13
IPSL-CM5A-LR	PISCES	31	-322	0.5–2˚	S14
IPSL-CM5A-MR	PISCES	31	-254	0.5–2˚	S14
MPI-ESM-LR	HAMOCC5.2	40	-249	1.5˚	S15
MPI-ESM-MR	HAMOCC5.2	40	-229	0.4˚	S15
NorESM1-ME	HAMOCC5.1	53	-206	1.125˚	S16
CESM1-BGC $\Delta r_{-O2:C}$= -0.2	BEC	60	382	1.125˚/0.27˚-0.53˚	This study
CESM1-BGC $\Delta r_{-O2:C}$= -0.1	BEC	60	186	1.125˚/0.27˚-0.53˚	This study
CESM1-BGC $\Delta r_{-O2:C}$= 0	BEC	60	0	1.125˚/0.27˚-0.53˚	This study
CESM1-BGC $\Delta r_{-O2:C}$= 0.1	BEC	60	-177	1.125˚/0.27˚-0.53˚	This study
CESM1-BGC $\Delta r_{-O2:C}$= 0.2	BEC	60	-308	1.125˚/0.27˚-0.53˚	This study
CESM1-BGC $\Delta r_{-O2:C}$= 0.3	BEC	60	-493	1.125˚/0.27˚-0.53˚	This study

Table S2.

Regional environmental characteristics. Observed environmental conditions in each defined biome [mean (minimum – maximum)].

Region	Stations	Temperature	Nutricline	N*
1: CAMR	1 - 13	28.4 (26.5 -29.5)	54.3 (1.9 - 92.4)	-1.66 (-3.5 – 0.50)
2: PNEC	14 - 26	28.5 (27.8 - 29.6)	40.9 (32.1 - 52.2)	0.44 (-0.30 – 1.14)
3: TPEQ	27 - 37	26.4 (25.9 - 27.7)	54.0 (32.1 - 67.2)	0.18 (-0.80 – 0.82)
4: PEQD	38 - 82	24.0 (21.6 - 25.7)	2.7 (1.9 - 32.1)	-1.16 (-3.39 – 0.27)
5: SPSG	83 - 121	23.4 (20.3 - 25.3)	164.3 (1.9 - 223.1)	-0.93 (-.3.50 – 0.82)
6: SSTC	122 - 144	14.8 (11.5 - 19.8)	1.9	-1.33 (-3.02 – -0.16)
7: SANT	145 - 170	8.6 (6.2 - 10.9)	1.9	0.30 (-1.15 – 1.41)
8: ANTA	171 - 187	3.6 (2.0 - 5.9)	1.9	2.00 (0.81 – 4.13)
9: APLR	188 - 198	0.7 (0 - 1.7)	1.9	1.91 (1.50 – 3.02)

Table S3.

The respiration quotient across regions.

Region	Average	Range	Standard Error	n
1: CAMR	1.26	1.10 – 1.48	0.036	13
2: PNEC	1.19	1.08 – 1.35	0.022	13
3: TPEQ	1.20	1.10 – 1.38	0.029	11
4: PEQD	1.15	0.98 - 1.43	0.011	45
5: SPSG	1.18	0.73 – 1.54	0.026	39
6: SSTC	1.14	0.75 – 1.54	0.027	23
7: SANT	1.13	0.99 – 1.33	0.017	26
8: ANTA	1.05	0.89 – 1.32	0.028	17
9: APLR	0.99	0.79 – 1.18	0.042	11

Table S4.

Statistical $r\text{-}_{O2:C}$ models. SE represents the coefficient of variation.

	Intercept	SE	Temperature	SE	Nutricline	SE	Phosphate	SE	N*	SE
$r\text{-}_{O2:C}$(T, $Z_{NO3,}$ P, N*)	1.10	8.3e-2	3.8e-3	2.6e-3	1.1e-4	1.7e-4	-3.4e-1	5.1e-2	1.8e-3	7.5e
$r\text{-}_{O2:C}$(T, $Z_{NO3,}$ P)	1.10	5.9e-2	3.7e-3*	1.8e-4	1.1e-4	1.6e-4	-3.2e-2	3.6e-2		
$r\text{-}_{O2:C}$(T, Z_{NO3}, N*)	1.04	2.2e-2	5.3e-3*	1.3e-3	1.7e-4	1.4e-4			2.4e-3	7.5e
$r\text{-}_{O2:C}$(T, P, N*)	1.13	7.1e-2	3.2e-3	2.4e-3			-5.1e-2	4.2e-2	1.8e-3	7.5e
$r\text{-}_{O2:C}$(Z_{NO3}, P, N*)	1.22	2.5e-2			2.6e-5	1.6e-4	-9.9e-2*	2.5e-2	-2.5e-3	7.0e
$r\text{-}_{O2:C}$(T, Z_{NO3})	1.05	1.9e-2	5.0e-3*	1.0e-3	1.8e-4	1.4e-4				
$r\text{-}_{O2:C}$(T, P)	1.12	5.3e-2	3.4e-3*	1.7e-3			-4.5e-2	3.2e-2		
$r\text{-}_{O2:C}$(T, N*)	1.04	2.2e-2	5.9e-3*	1.1e-3					3.2e-3	7.5e
$r\text{-}_{O2:C}$(Z_{NO3}, P)	1.21	2.1e-2			5.1e-5	1.6e-4	-9.4e-2*	2.1e-2		
$r\text{-}_{O2:C}$(Z_{NO3}, N*)	1.13	4.1e-2			4.0e-4*	1.4e-4			-1.6e-2*	6.4e
$r\text{-}_{O2:C}$(P, N*)	1.22	1.8e-2					-1.0e-1*	2.0e-1	-2.3e-3	6.9e
$r\text{-}_{O2:C}$(T)	1.05	1.9e-2	5.5e-3*	9.3e-4						
$r\text{-}_{O2:C}$(Z_{NO3})	1.13	1.0e-2			4.7e-4*	1.3e-4				
$r\text{-}_{O2:C}$(P)	1.22	1.5e-2					-9.8e-1*	1.7e-2		
$r\text{-}_{O2:C}$(N*)	1.14	9.2e-3							-1.9e-2*	6.4e

***p<0.05**

Table S5.

Values of the quantities used to standardize the sea surface temperature (*SST*) and the sea surface nitrate concentration (*SSN*). The means and standard-deviations use an area weighting based on the grid-boxes of our model.

	***SST* (°C)**	***SSN* (mmol/m^3)**
μ	18.1	5.37
std	9.78	15.2
MAX - MIN	31.5	48.6

Table S6.

Summary of the marginalized posterior distributions for the model with $\mathrm{r}_{-\mathrm{O2:C}} = mSST + b$ and with $\mathrm{r}_{-\mathrm{O2:C}} = mSSN + b$. The most probable value of each parameter is given along with their approximate 95% probability interval.

$\mathbf{r}_{-\mathbf{O2:C}} = \boldsymbol{mSST} + \boldsymbol{b}$		
Parameter	**Most probable value**	**95% probability interval**
$\boldsymbol{m}$	0.0162 (°C)$^{-1}$	(0.0155, 0.0168) (°C)$^{-1}$
$\boldsymbol{b}$	0.7310	(0.7213, 0.7406)
$\boldsymbol{\kappa_{dC}}^{-1}$	393.0 days	(391.6, 394.2) days
$\boldsymbol{\sigma}$	0.2192	(0.2149, 0.2237)
$\boldsymbol{b_C}$	1.1360	(1.1312, 1.1387)
$\boldsymbol{b_O}$	1.0234	(1.0215, 1.1370)
$\mathbf{r}_{-\mathbf{O2:C}} = \boldsymbol{mSSN} + \boldsymbol{b}$		
Parameter	**Most probable value**	**95% probability interval**
$\boldsymbol{m}$	-0.006949 (mmol/m^3)$^{-1}$	(-0.007903, -0.005995) (mmol/m^3)$^{-1}$
$\boldsymbol{b}$	1.0114	(1.0028, 1.0199)
$\boldsymbol{\kappa_{dC}}^{-1}$	395.3 days	(394.1, 396.6) days
$\boldsymbol{\sigma}$	0.1397	(0.1359, 0.14419)
$\boldsymbol{b_C}$	1.1979	(1.19427, 1.2016)
$\boldsymbol{b_O}$	1.0529	(1.0509, 1.2002)

Table S7.

Correlation comparison of the posterior probability distribution of the parameters for modal A ($r_{-O2:C} = mSST + b$) and model B ($r_{-O2:C} = mSSN + b$).

Model A:

	m	b	$\log \kappa_{dC}$	$\log \sigma$	$\log b_C$	$\log b_O$
$\boldsymbol{m}$	1	0.4135	0.1315	0.5192	−0.4952	−0.4200
$\boldsymbol{b}$	0.4135	1	0.4243	0.8592	−0.8304	0.1385
$\boldsymbol{\log \kappa_{dC}}$	0.1315	0.4243	1	0.3943	−0.4241	−0.3373
$\boldsymbol{\log \sigma}$	0.5192	0.8592	0.3943	1	−0.9612	0.3373
$\boldsymbol{\log b_C}$	−0.4952	−0.8304	−0.4241	−0.9612	1	0.3373
$\boldsymbol{\log b_O}$	−0.4200	0.1385	−0.0521	−0.3558	0.3373	1

Model B:

	$\boldsymbol{m}$	$\boldsymbol{b}$	$\boldsymbol{\log \kappa_{dC}}$	$\boldsymbol{\log \sigma}$	$\boldsymbol{\log b_C}$	$\boldsymbol{\log b_O}$
$\boldsymbol{m}$	1	−0.1641	−0.0444	−0.1799	−0.1701	0.4858
$\boldsymbol{b}$	−0.1641	1	0.4358	0.8352	−0.8026	0.2053
$\boldsymbol{\log \kappa_{dC}}$	−0.0444	0.4358	1	0.4099	−0.4385	−0.0421
$\boldsymbol{\log \sigma}$	−0.1799	0.8352	0.4099	1	−0.9545	−0.2789
$\boldsymbol{\log b_C}$	0.1701	−0.8026	−0.4385	−0.9545	1	0.2631
$\boldsymbol{\log b_O}$	0.4858	0.2053	−0.0421	−0.2789	0.2631	1

Table S8.

Globally integrated budgets of carbon respiration rate, oxygen consumption rate and nitrate consumption rate.

Model A	
Organic carbon respiration rate:	1.078 x 10^{15} mole/year
Oxygen consumption rate due to the oxidization of DOC: due to the oxidation of DON: Nitrate consumption rate:	 1.084 x 10^{15} mole/year 3.0928 x 10^{14} mole/year 1.350402 x 10^{13} mole/year
Model B	
Organic carbon respiration rate:	1.100 x 10^{15} mole/year
Oxygen consumption rate due to the oxidization of DOC: due to the oxidation of DON: Nitrate consumption rate:	 1.084 x 10^{15} mole/year 3.0928 x 10^{14} mole/year 1.350402 x 10^{13} mole/year

SI References

S1. D.S., S. & Skilling, J. Data Analysis A Bayesian Tutorial Second Edition (Oxford University Press, 2006).

S2. Wang, W. L., J. K. Moore, A. C. Martiny, F. W. Primeau, Convergent estimates of marine nitrogen fixation. *Nature* 566, 205–211 (2019).

S3. Primeau, F. W., M. Holzer, T. DeVries, Southern Ocean nutrient trapping and the efficiency of the biological pump. *J. Geophys. Res. Ocean.* 118, 2547–2564 (2013).

S4. Lewis, E. & Wallace, D.W.R. Program developed for CO2 system calculations (1998).

S5. van Heuven, S., Pierrot, D., Rae, J., Lewis, E. & Wallace, D. Matlab program developed for co2 system calculations. (2011).

S6. Key, R. M. *et al.*, Global Ocean Data Analysis Project, Version 2 (GLODAPv2) (2015).

S7. Letscher, R. T., Moore, J. K., Teng, Y. C. & Primeau, F. Variable C : N: P stoichiometry of dissolved organic matter cycling in the Community Earth System Model. Biogeosciences 12, 209—221 (2015).

S9. Finkel, Z. V *et al.*, Phylogenetic diversity in the macromolecular composition of microalgae. *PLoS One* **11**, e0155977 (2016).

S10. Chen, C. T. A., C. M. Lin, B. T. Huang, L. F. Chang, Stoichiometry of carbon, hydrogen, nitrogen, sulfur and oxygen in the particulate matter of the western North Pacific marginal seas. *Mar. Chem.* **54**, 179–190 (1996).

S11. Moore, J. K., S. C. Doney, J. A. Kleypas, D. M. Glover, I. Y. Fung, An intermediate complexity marine ecosystem model for the global domain. *Deep Sea Res. Part II Top. Stud. Oceanogr.* **49**, 403–462 (2002).

S12. Dunne, J. P. *et al.*, GFDL's ESM2 global coupled climate-carbon earth system models. Part II: Carbon system formulation and baseline simulation characteristics. *J. Clim.* **26**, 2247–2267 (2013).

S13. Palmer, J. R. ,I. J. Totterdell, Production and export in a global ocean ecosystem model. *Deep. Res.* **48**, 1169–1198 (2001).

S14. Aumont, O., L. Bopp, Globalizing results from ocean in situ iron fertilization studies. *Global Biogeochem. Cycles* **20** (2006).

S15. Ilyina, T. *et al.*, Global ocean biogeochemistry model HAMOCC: Model architecture and performance as component of the MPI-Earth system model in different CMIP5 experimental realizations. *J. Adv. Model. Earth Syst.* **5**, 287–315 (2013).

S16. Tjiputra, J. F. *et al.*, Evaluation of the carbon cycle components in the Norwegian Earth System Model (NorESM). *Geosci. Model Dev.* **6**, 301–325 (2013).

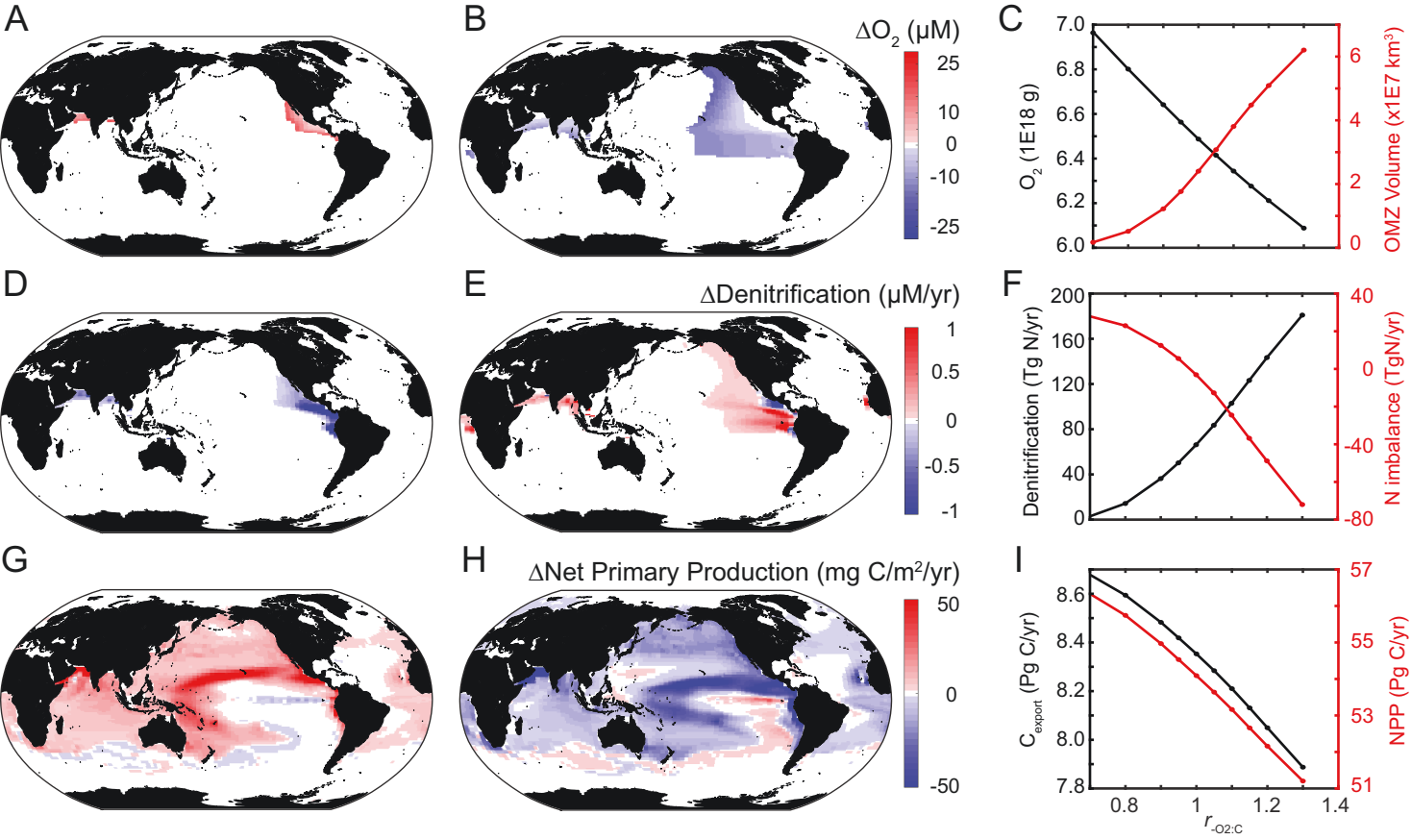
A
B
ΔO2 (μM)
25
10
0
-10
-25
C
7.0
6.8
6.6
6.4
6.2
6.0
O2 (1E18 g)
6
4
2
0
OMZ Volume (x1E7 km3)
D
E
ΔDenitrification (μM/yr)
1
0.5
0
-0.5
-1
F
200
160
120
80
40
0
Denitrification (Tg N/yr)
40
0
-40
-80
N imbalance (TgN/yr)
G
H
ΔNet Primary Production (mg C/m2/yr)
50
0
-50
I
8.6
8.4
8.2
8.0
7.8
Cexport (Pg C/yr)
57
55
53
51
NPP (Pg C/yr)
0.8
1
1.2
1.4
r-O2:C

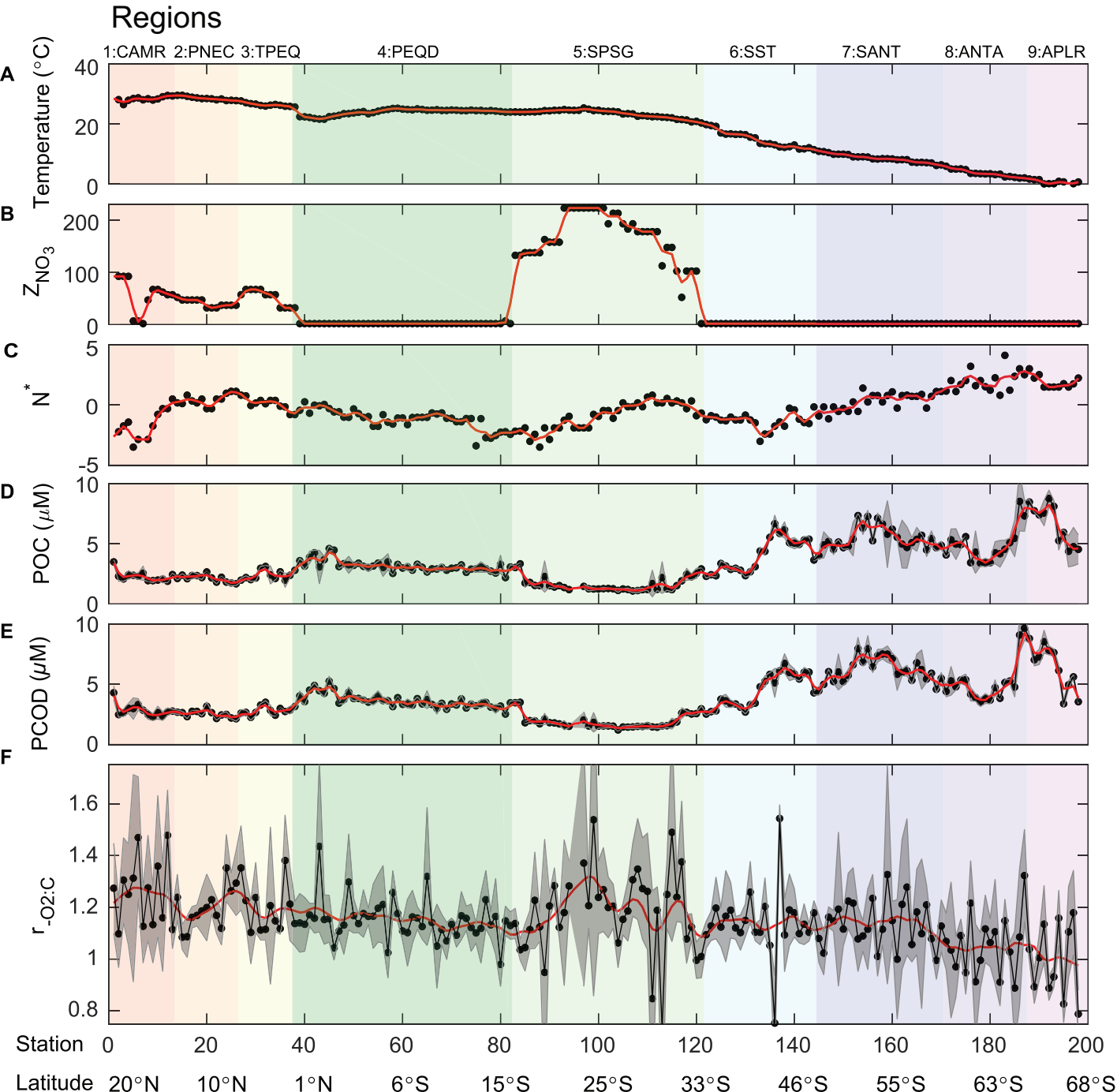
Regions
1:CAMR
2:PNEC
3:TPEQ
4:PEQD
5:SPSG
6:SST
7:SANT
8:ANTA
9:APLR
A
Temperature (°C)
B
Z_{NO_3}
C
N*
D
POC (μM)
E
PCOD (μM)
F
$r_{-O2:C}$
Station
Latitude
20°N
10°N
1°N
6°S
15°S
25°S
33°S
46°S
55°S
63°S
68°S

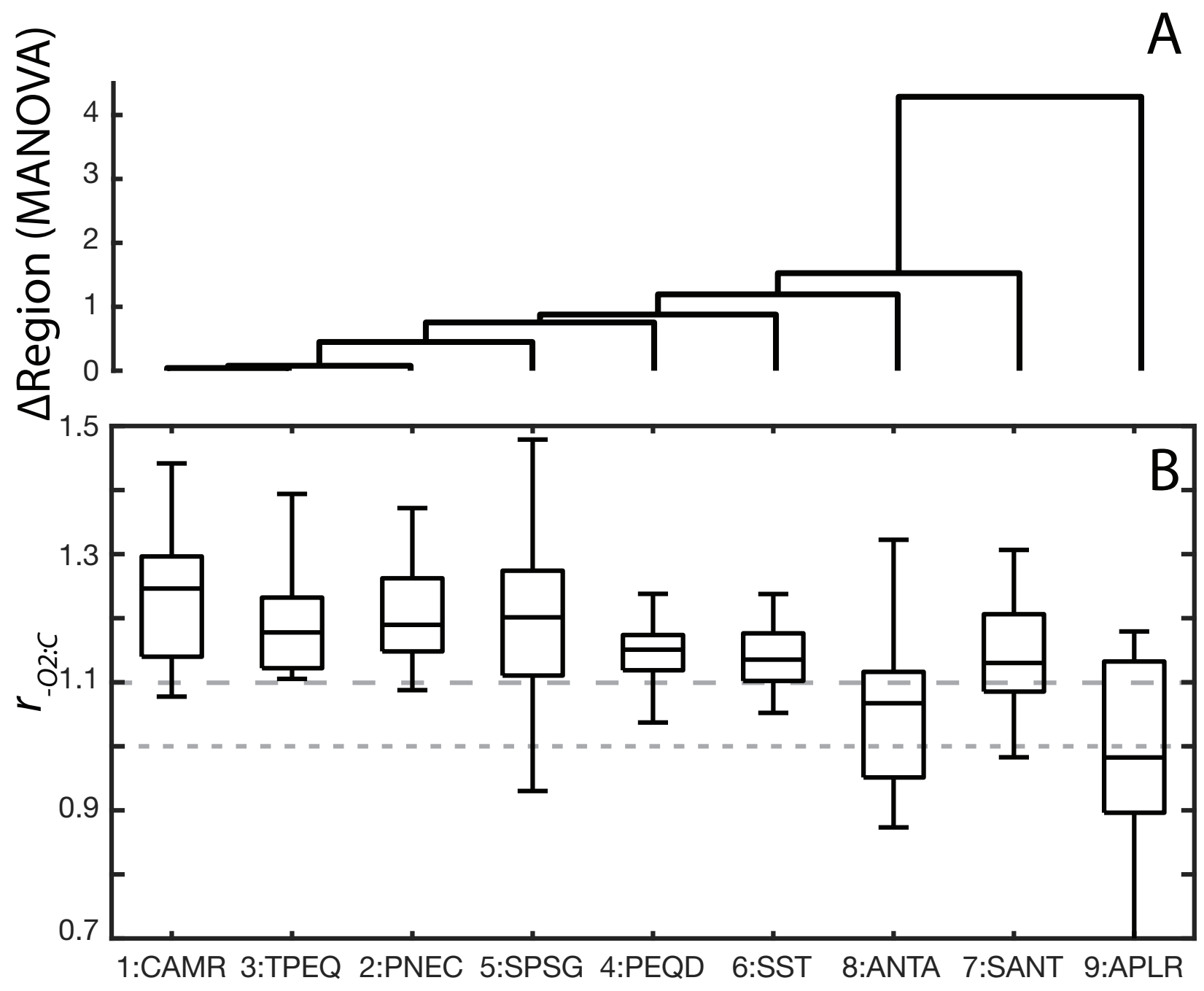
A
ΔRegion (MANOVA)
0
1
2
3
4
B
$r_{-O2:C}$
0.7
0.9
1.1
1.3
1.5
1:CAMR
3:TPEQ
2:PNEC
5:SPSG
4:PEQD
6:SST
8:ANTA
7:SANT
9:APLR

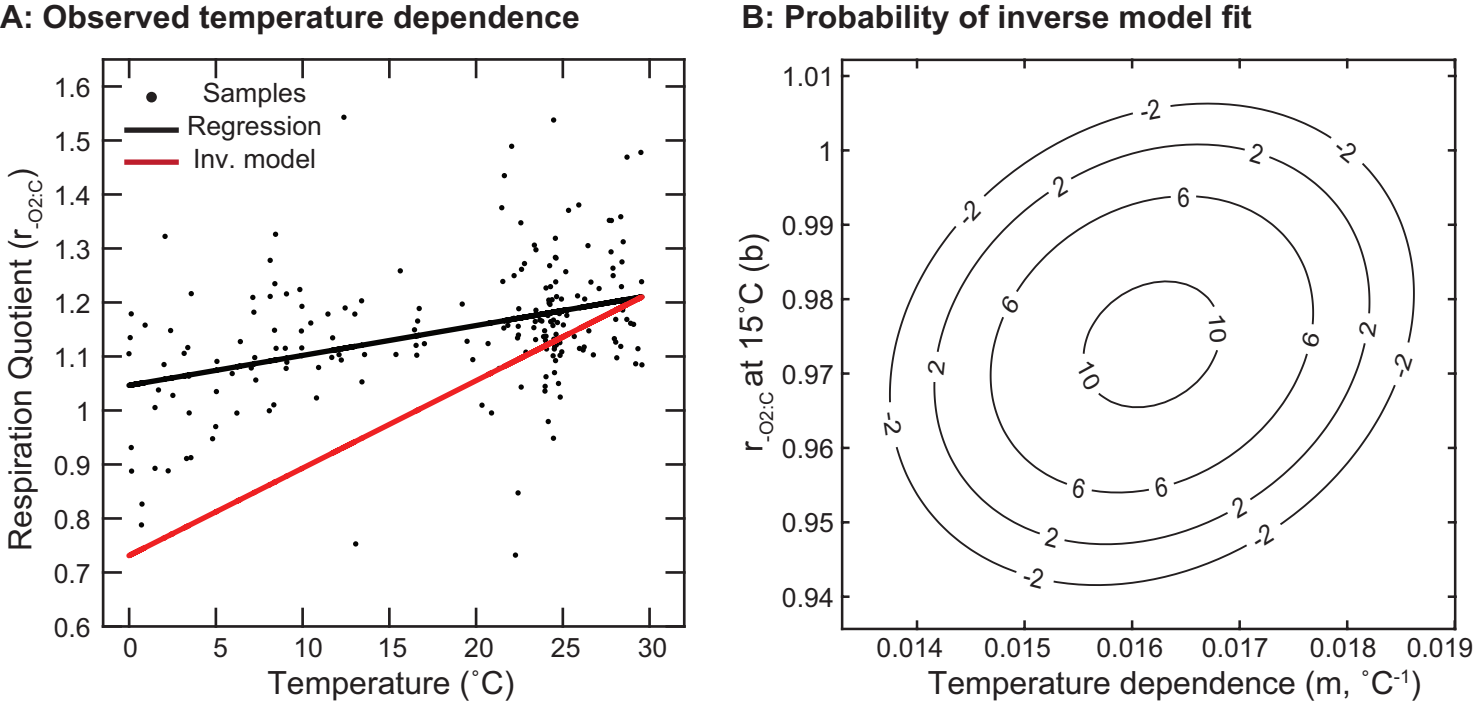
A: Observed temperature dependence
Samples
Regression
Inv. model
Respiration Quotient ($r_{-O2:C}$)
Temperature (˚C)
B: Probability of inverse model fit
$r_{-O2:C}$ at 15˚C (b)
Temperature dependence (m, ˚C^{-1})